SANDIA REPORT

SAND2006-4170
Unlimited Release
Printed August 2006

On the Formulation of a Crystal Plasticity Model

E.B. Marin

Prepared by
Sandia National Laboratories
Albuquerque, New Mexico 87185 and Livermore, California 94550

Sandia is a multiprogram laboratory operated by Sandia Corporation,
a Lockheed Martin Company, for the United States Department of Energy's
National Nuclear Security Administration under Contract DE-AC04-94-AL85000.

Sandia National Laboratories

Issued by Sandia National Laboratories, operated for the United States Department of Energy by Sandia Corporation.

Available to DOE and DOE contractors from
U.S. Department of Energy
Office of Scientific and Technical Information
P.O. Box 62
Oak Ridge, TN 37831

Telephone: (865) 576-8401
Facsimile: (865) 576-5728
E-Mail: reports@adonis.osti.gov
Online ordering: http://www.doe.gov/bridge

Available to the public from
U.S. Department of Commerce
National Technical Information Service
5285 Port Royal Rd
Springfield, VA 22161

Telephone: (800) 553-6847
Facsimile: (703) 605-6900
E-Mail: orders@ntis.fedworld.gov
Online order: http://www.ntis.gov/help/ordermethods.asp?loc=7-4-0#online

SAND2006-4170
Unlimited Release
Printed August 2006

On the Formulation of a Crystal Plasticity Model

E.B. Marin
Mechanics of Materials
Sandia National Laboratories
Livermore, CA 94551

Abstract

This report presents the formulation of a crystal elasto-viscoplastic model and the corresponding integration scheme. The model is suitable to represent the isothermal, anisotropic, large deformation of polycyrstalline metals. The formulation is an extension of a rigid viscoplastic model to account for elasticity effects, and incorporates a number of changes with respect to a previous formulation [Marin & Dawson, 1998]. This extension is formally derived using the well-known multiplicative decomposition of the deformation gradient into an elastic and plastic components, where the elastic part is additionally decomposed into the elastic stretch $\boldsymbol{V}^{e}$ and the proper orthogonal $\boldsymbol{R}^{e}$ tensors. The constitutive equations are written in the intermediate, stress-free configuration obtained by unloading the deformed crystal through the elastic stretch $\boldsymbol{V}^{e-1}$. The model is framed in a thermodynamic setting, and developed initially for large elastic strains. The crystal equations are then specialized to the case of small elastic strains, an assumption typically valid for metals. The developed integration scheme is implicit and proceeds by separating the spherical and deviatoric crystal responses. An "approximate" algorithmic material moduli is also derived for applications in implicit numerical codes. The model equations and their integration procedure have been implemented in both a material point simulator and a commercial finite element code. Both implementations are validated by solving a number of examples involving aggregates of either face centered cubic (FCC) or hexagonal close-packed (HCP) crystals subjected to different loading paths.

Keywords: crystal plasticity, finite deformation, constitutive integration, texture.

This page intentionally left blank.

Contents

List of Figures

List of Tables

1. Introduction

Crystal plasticity theories [Asaro, 1983], [Kocks, *et al.*, 1998] form the basis of grain-level (mesoscale) approaches to materials modeling using multi–scale strategies. A main feature of these theories is that they explicitly model discrete grains and slip systems, accounting then naturally for the anisotropy of single crystal properties and texture evolution, main contributors to the anisotropic macroscopic response of crystalline solids. Because these theories use a large number of internal state variables to represent the state of the material, they are computationally more expensive than macroscopic plasticity models. This aspect has limited their widespread use in the solution of system level engineering problems. However, as a mesoscale approach, these theories provide a very predictive and robust theoretical framework to get a better understanding of polycrystal behavior that can lead to better continuum plasticity models.

In this work, we present the formulation of a crystal plasticity model to describe the isothermal, quasi-static, large deformation of polycrystalline metals. The model is formulated based on the multiplicative decompositon of the deformation gradient into elastic and plastic components, a description physically motivated by the mechanisms underlying plastic slip in single crystals. The crystal constitutive equations are expressed in a relaxed configuration obtained by elastically unloading the deformed crystal without rotation from the current configuration to a stress-free state. These equations which are thermodynamically framed are derived for finite elasticity and then specialized to the case of small elastic strains. This simplification is introduced because metals, our main interest here, typically exhibit elastic strains that are orders of magnitude less than plastic strains in well–developed plastic flow. It is important to note that a formulation following similar guidelines has been previously used to develop a crystal plasticity model [Marin & Dawson, 1998]. However, the current development introduces a number of changes in the definition of some of the kinematic quantities, resulting in constitutive equations whose numerical treatment parallels many well-known integration procedures used in continuum plasticity [Simo & Hughes, 1998]. Such time integration of the model, which is implicit, is presented in detail along with the derivation of the material tangent moduli for use in implicit finite element codes. The performance of this integration scheme is evaluated by solving for the deformation of FCC and HCP crystal aggregates. Both a material point simulator and the commercial code *Abaqus* [ABAQUS, 2004] are used for this purpose.

The presentation begins with a description of the kinematics and thermodynamics used to formulate the crystal constitutive equations. The equations, initially derived for large

elastic strains, are then simplified using the small elastic strain assumption. This is followed by the description of the time integration of the crystal equations and the derivation of an approximate material tangent moduli. Applications of the model and its numerical implementation are then presented and discussed.

The work uses direct notation to express tensor quantities and their mathematical operations, with bold face letters being used to denote tensors. Consider. for example, two vectors $\boldsymbol{a}$ and $\boldsymbol{b}$, two second–order tensors $\boldsymbol{A}$ and $\boldsymbol{B}$, and the fourth–order tensor $\mathbb{C}$. The dyadic product of two vectors is indicated as $\boldsymbol{a} \otimes \boldsymbol{b}$ (a second–order tensor) and the contraction of a second–order tensor with a vector as $\boldsymbol{A}\boldsymbol{a}$ (a vector). Tensor operations between two second–order tensors are represented as $\boldsymbol{A}\boldsymbol{B}$ for the inner product (a second–order tensor), $\boldsymbol{A} \otimes \boldsymbol{B}$ for the dyadic product (a fourth–order tensor), and $\boldsymbol{A}\!:\!\boldsymbol{B}$ for the scalar product (a scalar). The contraction operation over two indices between a fourth–order tensor and a second order tensor is denoted as $\mathbb{C}\!:\!\boldsymbol{A}$. Any other particular tensor notation/operation used in the development will be either clear from the context or indicated in the text.

2. Model Formulation

2.1 Kinematics.

The elasto-plastic response of single crystals is modeled assuming that crystallographic slip is the dominant deformation mechanism. Other mechanisms such as twinning, grain boundary sliding, and diffusion are not considered in this development. The single crystal kinematics can then be described based on the local multiplicative decomposition of the deformation gradient $\boldsymbol{F}$ into an elastic, $\boldsymbol{F}^e$ and a plastic, $\boldsymbol{F}^p$, component. In addition, the elastic component $\boldsymbol{F}^e$ is decomposed into the symmetric left elastic stretch tensor $\boldsymbol{V}^e$ and the proper orthogonal (rotation) tensor $\boldsymbol{R}^e$ ($\det \boldsymbol{R}^e = 1$), see Fig. 2.1. Thus, the kinematics of a single crystal can be expressed as

$$\boldsymbol{F} = \boldsymbol{V}^e \boldsymbol{F}^\star, \qquad \boldsymbol{F}^\star = \boldsymbol{R}^e \boldsymbol{F}^p \tag{2.1}$$

where $\det \boldsymbol{F}^\star = \det \boldsymbol{F}^p = 1$ and $\det \boldsymbol{F} = \det \boldsymbol{V}^e > 0$. Here $\boldsymbol{F}^p$ describes the motion of dislocations (plastic slip) on crystallographic planes (slip planes) leaving the crystal lattice unchanged, while $\boldsymbol{R}^e$ and $\boldsymbol{V}^e$ model the rotation and the elastic stretching of the lattice, respectively. The decomposition (2.1) introduces two intermediate configurations between the undeformed ($\mathcal{B}_0$) and the current ($\mathcal{B}$) configurations, which are denoted here as $\bar{\mathcal{B}}$ and $\widetilde{\mathcal{B}}$. These configurations are respectively defined by $\boldsymbol{F}^p$ and $\boldsymbol{F}^\star$ and are typically used in the constitutive description of single crystals [Kalidindi, *et al.*, 1992], [Cuitiño & Ortiz, 1992], [Marin & Dawson, 1998]. In this work, we will use the relaxed configuration $\widetilde{\mathcal{B}}$ to write the crystal constitutive equations. Hypothetically, this configuration is obtained by elastically unloading through $\boldsymbol{V}^{e-1}$ without rotation from the current configuration to a stress free state.

Using the kinematic decomposition (2.1), we can write the velocity gradient $\boldsymbol{l}$ in $\mathcal{B}$ as

$$\boldsymbol{l} = \dot{\boldsymbol{F}}\boldsymbol{F}^{-1} = \dot{\boldsymbol{V}}^e \boldsymbol{V}^{e-1} + \boldsymbol{V}^e \widetilde{\boldsymbol{L}}^\star \boldsymbol{V}^{e-1}, \qquad \widetilde{\boldsymbol{L}}^\star = \dot{\boldsymbol{F}}^\star \boldsymbol{F}^{\star-1} = \dot{\boldsymbol{R}}^e \boldsymbol{R}^{eT} + \boldsymbol{R}^e \bar{\boldsymbol{L}}^p \boldsymbol{R}^{eT}, \tag{2.2}$$

where $\bar{\boldsymbol{L}}^p = \dot{\boldsymbol{F}}^p \boldsymbol{F}^{p-1} = \sum_{\alpha=1}^{N} \dot{\gamma}^\alpha \bar{\boldsymbol{s}}^\alpha \otimes \bar{\boldsymbol{m}}^\alpha$ is the plastic velocity gradient as given in $\bar{\mathcal{B}}$. Here, $\dot{\gamma}^\alpha$ is the plastic shearing rate on the α–slip system, and the unit vectors $(\bar{\boldsymbol{s}}^\alpha, \bar{\boldsymbol{m}}^\alpha)$ define the orientation of the α–slip system in $\bar{\mathcal{B}}$ through the dyadic product $\bar{\boldsymbol{Z}}^\alpha = \bar{\boldsymbol{s}}^\alpha \otimes \bar{\boldsymbol{m}}^\alpha$, the Schmid tensor. The summation is performed over the N potentially slip systems. Note that by the constitutive assumption introduced for $\dot{\boldsymbol{F}}^p \boldsymbol{F}^{p-1}$, the multiplicative decomposition given by

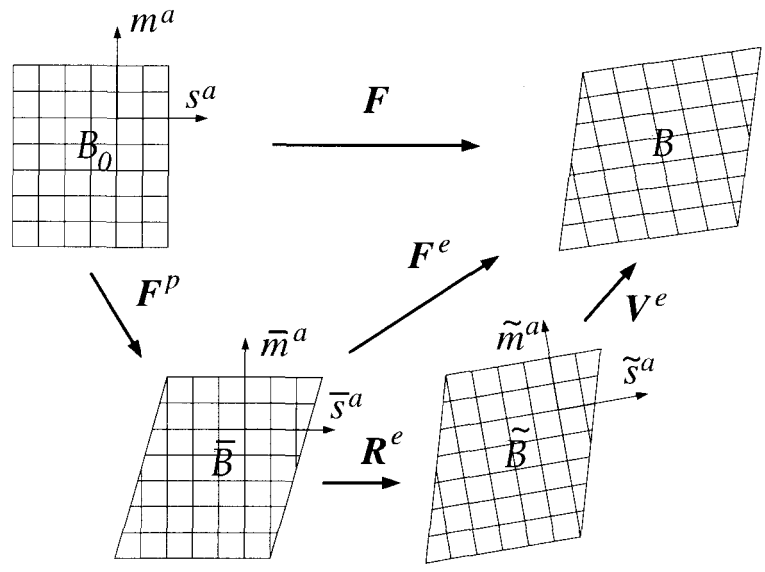

Figure 2.1: Kinematics of elasto-plastic deformation of single crystals deforming by crystallographic slip: $\boldsymbol{F} = \boldsymbol{F}^e\boldsymbol{F}^p$ with $\boldsymbol{F}^e = \boldsymbol{V}^e\boldsymbol{R}^e$. The intermediate configuration $\tilde{\mathcal{B}}$ is defined by elastically unloading the current configuration $\mathcal{B}$ through the elastic stretch $\boldsymbol{V}^{e-1}$. The crystal constitutive equations are written with respect to $\tilde{\mathcal{B}}$.

Eq.(2.1) is unique. By denoting $\tilde{\boldsymbol{\Omega}}^e = \dot{\boldsymbol{R}}^e\boldsymbol{R}^{eT}$, the spin of the lattice, we can alternatively express Eq.(2.2) in configuration $\tilde{\mathcal{B}}$ as

$$\tilde{\boldsymbol{L}} = \boldsymbol{V}^{e-1}\boldsymbol{l}\boldsymbol{V}^e = \boldsymbol{V}^{e-1}\dot{\boldsymbol{V}}^e + \tilde{\boldsymbol{L}}^\star, \qquad \tilde{\boldsymbol{L}}^\star = \tilde{\boldsymbol{\Omega}}^e + \sum_{\alpha=1}^{N} \dot{\gamma}^\alpha \tilde{\boldsymbol{s}}^\alpha \otimes \tilde{\boldsymbol{m}}^\alpha \tag{2.3}$$

where $\tilde{\boldsymbol{s}}^\alpha = \boldsymbol{R}^e\bar{\boldsymbol{s}}^\alpha$ and $\tilde{\boldsymbol{m}}^\alpha = \boldsymbol{R}^e\bar{\boldsymbol{m}}^\alpha$. Clearly, $\tilde{\boldsymbol{L}}^\star$ describes both the plastic flow due to crystallographic slip and the rotation of the lattice, as referred to the unloaded configuration $\tilde{\mathcal{B}}$. Note that for $\boldsymbol{V}^e = \boldsymbol{1}$, we obtain $\tilde{\boldsymbol{L}}^\star = \tilde{\boldsymbol{L}} = \boldsymbol{l}$ (configuration $\tilde{\mathcal{B}}$ and $\mathcal{B}$ are identical), and the kinematics above will describe the deformation of a rigid-viscoplastic crystal [Mathur & Dawson, 1989]. Hence, as proposed previously [Marin & Dawson, 1998], the current formulation can be regarded as an extension of a crystal rigid-viscoplastic model to include elasticity effects.

Using the decomposition $\boldsymbol{l} = \boldsymbol{d} + \boldsymbol{w}$, where $\boldsymbol{d} = \mathrm{sym}(\boldsymbol{l})$ and $\boldsymbol{w} = \mathrm{skew}(\boldsymbol{l})$ are the rate of deformation and spin tensors in $\mathcal{B}$, respectively, we can write the symmetric and skew parts of Eq.$(2.2)_1$ as

$$\boldsymbol{d} = \mathrm{sym}(\dot{\boldsymbol{V}}^e\boldsymbol{V}^{e-1}) + \boldsymbol{V}^{e-T}\tilde{\boldsymbol{D}}^\star\boldsymbol{V}^{e-1}, \tag{2.4}$$

$$\boldsymbol{w} = \mathrm{skew}(\dot{\boldsymbol{V}}^e\boldsymbol{V}^{e-1}) + \boldsymbol{V}^{e-T}\tilde{\boldsymbol{W}}^\star\boldsymbol{V}^{e-1} \tag{2.5}$$

where we have defined $\widetilde{\boldsymbol{D}}^{\star} = \mathrm{sym}(\widetilde{\boldsymbol{C}}^{e}\widetilde{\boldsymbol{L}}^{\star})$, $\widetilde{\boldsymbol{W}}^{\star} = \mathrm{skew}(\widetilde{\boldsymbol{C}}^{e}\widetilde{\boldsymbol{L}}^{\star})$. With the help of Eq.$(2.2)_2$, $\widetilde{\boldsymbol{D}}^{\star}$ and $\widetilde{\boldsymbol{W}}^{\star}$ can be expressed as

$$\widetilde{\boldsymbol{D}}^{\star} = \mathrm{sym}(\widetilde{\boldsymbol{C}}^{e}\widetilde{\boldsymbol{\Omega}}^{e}) + \boldsymbol{R}^{e}\bar{\boldsymbol{D}}^{p}\boldsymbol{R}^{eT}, \tag{2.6}$$

$$\widetilde{\boldsymbol{W}}^{\star} = \mathrm{skew}(\widetilde{\boldsymbol{C}}^{e}\widetilde{\boldsymbol{\Omega}}^{e}) + \boldsymbol{R}^{e}\bar{\boldsymbol{W}}^{p}\boldsymbol{R}^{eT} \tag{2.7}$$

where $\bar{\boldsymbol{D}}^{p} = \mathrm{sym}(\bar{\boldsymbol{C}}^{e}\bar{\boldsymbol{L}}^{p})$, and $\bar{\boldsymbol{W}}^{p} = \mathrm{skew}(\bar{\boldsymbol{C}}^{e}\bar{\boldsymbol{L}}^{p})$. Here $\widetilde{\boldsymbol{C}}^{e} = \boldsymbol{V}^{eT}\boldsymbol{V}^{e}$ and $\bar{\boldsymbol{C}}^{e} = \boldsymbol{F}^{eT}\boldsymbol{F}^{e}$ are the elastic right Cauchy-Green tensors in configurations $\widetilde{\mathcal{B}}$ and $\bar{\mathcal{B}}$, respectively, both of which are related by $\widetilde{\boldsymbol{C}}^{e} = \boldsymbol{R}^{e}\bar{\boldsymbol{C}}^{e}\boldsymbol{R}^{eT}$. Note that the rotation tensor $\boldsymbol{R}^{e}$ is uniquely defined by its evolution equation which can be obtained from Eqs.(2.5) and (2.7).

It is worthwhile to note that Eq.(2.4), which implicitly represents an additive decomposition in $\mathcal{B}$ of the rate of deformation tensor $\boldsymbol{d}$ into an elastic and a plastic components, can alternatively be written in configurations $\widetilde{\mathcal{B}}$ and $\bar{\mathcal{B}}$. To write this expression in configuration $\widetilde{\mathcal{B}}$, we use the definition for $\widetilde{\boldsymbol{L}}$ in Eq.(2.3), i.e. $\widetilde{\boldsymbol{L}} = \boldsymbol{V}^{e-1}\boldsymbol{l}\boldsymbol{V}^{e}$, together with $\widetilde{\boldsymbol{D}} = \mathrm{sym}(\widetilde{\boldsymbol{C}}^{e}\widetilde{\boldsymbol{L}})$ to obtain $\widetilde{\boldsymbol{D}} = \boldsymbol{V}^{e}\boldsymbol{d}\boldsymbol{V}^{e}$. Also, one can easily show that $\boldsymbol{V}^{eT}\mathrm{sym}(\dot{\boldsymbol{V}}^{e}\boldsymbol{V}^{e-1})\boldsymbol{V}^{e} = 1/2\dot{\widetilde{\boldsymbol{C}}}^{e} = \dot{\widetilde{\boldsymbol{E}}}^{e}$ where $\widetilde{\boldsymbol{E}}^{e} = 1/2(\widetilde{\boldsymbol{C}}^{e} - \boldsymbol{1})$. Substituting these expressions in Eq.(2.4) and using Eq.(2.6), one can then write the referred additive decomposition in $\widetilde{\mathcal{B}}$ as

$$\widetilde{\boldsymbol{D}} = \dot{\widetilde{\boldsymbol{E}}}^{e} + \widetilde{\boldsymbol{D}}^{\star} \qquad \text{or} \qquad \widetilde{\boldsymbol{D}} = \overset{\nabla}{\widetilde{\boldsymbol{E}}}^{e} + \boldsymbol{R}^{e}\bar{\boldsymbol{D}}^{p}\boldsymbol{R}^{eT} \tag{2.8}$$

where $\overset{\nabla}{\widetilde{\boldsymbol{E}}}^{e} = \dot{\widetilde{\boldsymbol{E}}}^{e} + \widetilde{\boldsymbol{E}}^{e}\widetilde{\boldsymbol{\Omega}}^{e} - \widetilde{\boldsymbol{\Omega}}^{e}\widetilde{\boldsymbol{E}}^{e}$ is a Green-McInnis-Naghdi rate type of $\widetilde{\boldsymbol{E}}^{e}$ based on the lattice (elastic) spin $\widetilde{\boldsymbol{\Omega}}^{e}$. Note that this corrotational rate arises naturally in the formulation. Using $\widetilde{\boldsymbol{\Omega}}^{e} = \dot{\boldsymbol{R}}^{e}\boldsymbol{R}^{eT}$, one can also write this objective rate as

$$\overset{\nabla}{\widetilde{\boldsymbol{E}}}^{e} = \boldsymbol{R}^{e}\left[\frac{\partial}{\partial t}(\underbrace{\boldsymbol{R}^{eT}\widetilde{\boldsymbol{E}}^{e}\boldsymbol{R}^{e}}_{\bar{\boldsymbol{E}}^{e}})\right]\boldsymbol{R}^{eT} = \boldsymbol{R}^{e}\dot{\bar{\boldsymbol{E}}}^{e}\boldsymbol{R}^{eT} \tag{2.9}$$

where $\bar{\boldsymbol{E}}^{e} = 1/2(\boldsymbol{C}^{e} - \boldsymbol{1})$. On the other hand, the additive decomposition of the rate of deformation tensors in configuration $\bar{\mathcal{B}}$ can be obtained by substituting Eq.(2.9) into Eq.$(2.8)_2$ to yield

$$\bar{\boldsymbol{D}} = \dot{\bar{\boldsymbol{E}}}^{e} + \bar{\boldsymbol{D}}^{p} \tag{2.10}$$

where $\bar{\boldsymbol{D}} = \boldsymbol{R}^{eT}\widetilde{\boldsymbol{D}}\boldsymbol{R}^{e}$.

Remark 1. Consider the definition of the right Cauchy-Green tensor in configuration $\mathcal{B}_0$, i.e., $\boldsymbol{C} = \boldsymbol{F}^{T}\boldsymbol{F}$. We can then write

$$\boldsymbol{C} = \boldsymbol{F}^{T}\boldsymbol{F} = \boldsymbol{F}^{\star T}\underbrace{\boldsymbol{V}^{eT}\boldsymbol{V}^{e}}_{\widetilde{\boldsymbol{C}}^{e}}\boldsymbol{F}^{\star} \quad \rightarrow \quad \boldsymbol{C} = \boldsymbol{F}^{\star T}\widetilde{\boldsymbol{C}}^{e}\boldsymbol{F}^{\star} \tag{2.11}$$

where the multiplicative decomposition, Eq.(2.1)$_1$, has been used. By taking the time derivative of Eq.(2.11)$_2$ one can obtain after some algebra

$$\underbrace{\frac{1}{2}\boldsymbol{F}^{\star-T}\left[\frac{\partial}{\partial t}\boldsymbol{F}^{\star T}\widetilde{\boldsymbol{C}}^{e}\boldsymbol{F}^{\star})\right]\boldsymbol{F}^{\star-1}}_{\mathcal{L}_v^{\star}\widetilde{\boldsymbol{C}}^{e}} = \frac{1}{2}\dot{\widetilde{\boldsymbol{C}}}^{e} + \mathrm{sym}(\widetilde{\boldsymbol{C}}^{e}\widetilde{\boldsymbol{L}}^{\star}) \tag{2.12}$$

where $\mathcal{L}_v^{\star}\widetilde{\boldsymbol{C}}^{e}$ denotes the Lie time derivative of $\widetilde{\boldsymbol{C}}^{e}$ with respect to the deformation gradient $\boldsymbol{F}^{\star}$. Comparison of Eqs.(2.8)$_1$ and (2.12) provides an equivalent definition for $\widetilde{\boldsymbol{D}}$ as

$$\widetilde{\boldsymbol{D}} = \frac{1}{2}\mathcal{L}_v^{\star}\widetilde{\boldsymbol{C}}^{e} = \frac{1}{2}\boldsymbol{F}^{\star-T}\frac{\partial}{\partial t}\Big(\boldsymbol{F}^{\star T}\widetilde{\boldsymbol{C}}^{e}\boldsymbol{F}^{\star}\Big)\boldsymbol{F}^{\star-1} \tag{2.13}$$

A similar expression can be obtained for $\bar{\boldsymbol{D}}$ by replacing $\boldsymbol{F}^{\star}$ and $\widetilde{\boldsymbol{C}}^{e}$ with $\boldsymbol{F}^{p}$ and $\bar{\boldsymbol{C}}^{e}$, respectively, in Eqs.(2.11)$_2$–(2.13). This yields

$$\frac{1}{2}\mathcal{L}_v^{p}\bar{\boldsymbol{C}}^{e} = \frac{1}{2}\dot{\bar{\boldsymbol{C}}}^{e} + \mathrm{sym}(\bar{\boldsymbol{C}}^{e}\bar{\boldsymbol{L}}^{p}), \qquad \bar{\boldsymbol{D}} = \frac{1}{2}\mathcal{L}_v^{p}\bar{\boldsymbol{C}}^{e} = \frac{1}{2}\boldsymbol{F}^{p-T}\frac{\partial}{\partial t}\Big(\boldsymbol{F}^{pT}\bar{\boldsymbol{C}}^{e}\boldsymbol{F}^{p}\Big)\boldsymbol{F}^{p-1} \tag{2.14}$$

with $\mathcal{L}_v^{p}\bar{\boldsymbol{C}}^{e}$ being the plastic Lie time derivative of $\bar{\boldsymbol{C}}^{e}$.

2.2 Thermodynamics.

In this section, we frame the state variable model of crystal plasticity in the context of the thermodynamics proposed by [Coleman & Gurtin, 1967]. For this purpose, we write the mechanical version of the reduced entropy (Clasius-Duhem) inequality per unit volume of the unloaded intermediate configuration $\widetilde{\mathcal{B}}$ *

$$-\dot{\widetilde{\Psi}}_{\mathrm{v}} + \boldsymbol{\tau}\!:\!\boldsymbol{l} \geq 0 \tag{2.15}$$

where $\widetilde{\Psi}_{\mathrm{v}}$ is the Helmholtz free energy per unit volume in $\widetilde{\mathcal{B}}$ and $\boldsymbol{\tau} = (\det \boldsymbol{F})\boldsymbol{\sigma} = (\det \boldsymbol{F}^{e})\boldsymbol{\sigma}$ is the Kirchhoff stress, with $\boldsymbol{\sigma}$ being the Cauchy stress. Define $\widetilde{\boldsymbol{S}} = \boldsymbol{V}^{e-1}\boldsymbol{\tau}\boldsymbol{V}^{e-T}$ as the

*Denote the free energy per unit mass as Ψ_m and the free energy per unit volume V in $\mathcal{B}$ as Ψ_{v}. One can relate these quantities by

$$\int_{\mathcal{B}} \rho\Psi_m d\mathrm{V} = \int_{\mathcal{B}} \Psi_{\mathrm{v}} d\mathrm{V} = \int_{\widetilde{\mathcal{B}}} \widetilde{\Psi}_{\mathrm{v}} d\widetilde{\mathrm{V}}$$

where $\widetilde{\Psi}_{\mathrm{v}} = J^{e}\Psi_{\mathrm{v}}$ is the free energy per unit volume $\widetilde{\mathrm{V}}$ in $\widetilde{\mathcal{B}}$. The material time derivative of the last integral above can be evaluated as

$$\frac{D}{Dt}\int_{\widetilde{\mathcal{B}}} \widetilde{\Psi}_{\mathrm{v}} d\widetilde{\mathrm{V}} = \int_{\widetilde{\mathcal{B}}} \Big[\dot{\widetilde{\Psi}}_{\mathrm{v}} + \widetilde{\Psi}_{\mathrm{v}}\mathrm{tr}(\boldsymbol{L}^{\star})\Big] d\widetilde{\mathrm{V}} = \int_{\widetilde{\mathcal{B}}} \dot{\widetilde{\Psi}}_{\mathrm{v}} d\widetilde{\mathrm{V}}$$

since, from Eq.(2.2)$_2$, $\mathrm{tr}(\boldsymbol{L}^{\star}) = \mathrm{tr}(\widetilde{\boldsymbol{\Omega}}^{e}) + \mathrm{tr}(\bar{\boldsymbol{L}}^{p}) = 0$. In a similar fashion, one can write the stress power $\mathcal{P}_{int}$ as

$$\mathcal{P}_{int} = \int_{\mathcal{B}} \boldsymbol{\sigma}\!:\!\boldsymbol{l} d\mathrm{V} = \int_{\widetilde{\mathcal{B}}} J^{e}\boldsymbol{\sigma}\!:\!\boldsymbol{l} d\widetilde{\mathrm{V}} = \int_{\widetilde{\mathcal{B}}} \boldsymbol{\tau}\!:\!\boldsymbol{l} d\widetilde{\mathrm{V}}$$

where $\boldsymbol{\tau}\!:\!\boldsymbol{l}$ is the stress power per unit volume in $\widetilde{\mathcal{B}}$. By substituting the above two expressions in the first and second law of thermodynamics and considering only the mechanical part one obtains Eq.(2.15).

2nd Piola-Kirchhoff stress in $\widetilde{\mathcal{B}}$, and use $\boldsymbol{l} = \boldsymbol{V}^e \widetilde{\boldsymbol{L}} \boldsymbol{V}^{e-1}$, Eq.(2.3), to express Eq.(2.15) in configuration $\widetilde{\mathcal{B}}$ as

$$-\dot{\widetilde{\Psi}}_{\mathrm{v}} + \widetilde{\boldsymbol{C}}^e \widetilde{\boldsymbol{S}} : \widetilde{\boldsymbol{L}} \geq 0 \tag{2.16}$$

Note that the second term of this equation can be expressed as

$$\widetilde{\boldsymbol{C}}^e \widetilde{\boldsymbol{S}} : \widetilde{\boldsymbol{L}} = \widetilde{\boldsymbol{S}} : \widetilde{\boldsymbol{C}}^e \widetilde{\boldsymbol{L}} = \widetilde{\boldsymbol{S}} : \mathrm{sym}(\widetilde{\boldsymbol{C}}^e \widetilde{\boldsymbol{L}}) = \widetilde{\boldsymbol{S}} : \widetilde{\boldsymbol{D}} \tag{2.17}$$

where $\widetilde{\boldsymbol{D}}$ is given by Eq.(2.8). Then substituting Eqs.(2.17) and $(2.8)_2$ into Eq.(2.16), the reduced entropy inequality can be written as

$$-\dot{\widetilde{\Psi}}_{\mathrm{v}} + \widetilde{\boldsymbol{S}} : \overset{\nabla}{\widetilde{\boldsymbol{E}}}^e + \widetilde{\boldsymbol{S}} : (\boldsymbol{R}^e \bar{\boldsymbol{D}}^p \boldsymbol{R}^{eT}) \geq 0 \tag{2.18}$$

Here, it is assumed that the free energy depends upon the applied elastic strain $\widetilde{\boldsymbol{E}}^e$, and a set of strain-like internal state variables for each α–slip system $\widetilde{\boldsymbol{X}}^\alpha$, i.e.,

$$\widetilde{\Psi}_{\mathrm{v}} = \hat{\widetilde{\Psi}}_{\mathrm{v}}(\widetilde{\boldsymbol{E}}^e, \widetilde{\boldsymbol{X}}^\alpha) \tag{2.19}$$

Physically, the set $\widetilde{\boldsymbol{X}}^\alpha$ is incorporated to represent the state of the evolving internal structure of the material generated during plastic slip. In this work, we select a reduced set represented by the scalar state variables ϵ_s^α which are assumed to be related to the lattice strain fields around dislocations generated/accumulated on the α–slip system. These state variables will effectively model the isotropic hardening effects induced by the interaction among these dislocation internal elastic strain fields, and are connected to the density of (statistically stored) dislocations ρ_s^α by the relation $\epsilon_s^\alpha = b\sqrt{\rho_s^\alpha}$, where b is the Burger's vector. Thus, assuming $\widetilde{\boldsymbol{X}}^\alpha = \{\epsilon_s^\alpha\}$, we can compute the material time derivative of $\widetilde{\Psi}_{\mathrm{v}}$ as

$$\dot{\widetilde{\Psi}}_{\mathrm{v}} = \frac{\partial \widetilde{\Psi}_{\mathrm{v}}}{\partial \widetilde{\boldsymbol{E}}^e} : \overset{\nabla}{\widetilde{\boldsymbol{E}}}^e + \sum_{\alpha=1}^{N} \frac{\partial \widetilde{\Psi}_{\mathrm{v}}}{\partial \epsilon_s^\alpha} \dot{\epsilon}_s^\alpha \tag{2.20}$$

Upon substituting Eq.(2.20) into Eq.(2.18) yields

$$\Big(-\frac{\partial \widetilde{\Psi}_{\mathrm{v}}}{\partial \widetilde{\boldsymbol{E}}^e} + \widetilde{\boldsymbol{S}} \Big) : \overset{\nabla}{\widetilde{\boldsymbol{E}}}^e + \widetilde{\boldsymbol{S}} : (\boldsymbol{R}^e \bar{\boldsymbol{D}}^p \boldsymbol{R}^{eT}) - \sum_{\alpha=1}^{N} \underbrace{\frac{\partial \widetilde{\Psi}_{\mathrm{v}}}{\partial \epsilon_s^\alpha}}_{\kappa_s^\alpha} \dot{\epsilon}_s^\alpha \geq 0 \tag{2.21}$$

where κ_s^α, defined by

$$\kappa_s^\alpha = \frac{\partial \widetilde{\Psi}_{\mathrm{v}}}{\partial \epsilon_s^\alpha}, \tag{2.22}$$

is the stress–like internal state variable (flow strength) conjugate to the kinematic–like variable ϵ_s^α. As such, κ_s^α will represent the internal lattice stress fields generated by the dislocation

structures formed during plastic deformation. Following standard arguments, one can obtain from Eq.(2.21) the elastic constitutive law for $\widetilde{\boldsymbol{S}}$,

$$\widetilde{\boldsymbol{S}} = \frac{\partial \widetilde{\Psi}_{\mathrm{v}}}{\partial \widetilde{\boldsymbol{E}}^{e}} \tag{2.23}$$

Also, the second term on the left side of Eq.(2.21) can be written as

$$\widetilde{\boldsymbol{S}}{:}(\boldsymbol{R}^{e}\bar{\boldsymbol{D}}^{p}\boldsymbol{R}^{eT}) = \widetilde{\boldsymbol{S}}{:}\Big[\boldsymbol{R}^{e}\,\mathrm{sym}(\bar{\boldsymbol{C}}^{e}\bar{\boldsymbol{L}}^{p})\boldsymbol{R}^{eT}\Big] = \sum_{\alpha=1}^{N}\Big[\underbrace{\widetilde{\boldsymbol{S}}:\mathrm{sym}(\widetilde{\boldsymbol{C}}^{e}\widetilde{\boldsymbol{Z}}^{\alpha})}_{\tau^{\alpha}}\Big]\dot{\gamma}^{\alpha} \tag{2.24}$$

where we have used $\widetilde{\boldsymbol{C}}^{e} = \boldsymbol{R}^{e}\bar{\boldsymbol{C}}^{e}\boldsymbol{R}^{eT}$ and $\widetilde{\boldsymbol{Z}}^{\alpha} = \boldsymbol{R}^{e}\bar{\boldsymbol{Z}}^{\alpha}\boldsymbol{R}^{eT} = \widetilde{\boldsymbol{s}}^{\alpha}\otimes\widetilde{\boldsymbol{m}}^{\alpha}$, with $\widetilde{\boldsymbol{Z}}^{\alpha}$ being the Schmid tensor expressed in $\widetilde{\mathcal{B}}$. In this equation, τ^{α} is the resolve shear stress on the α–slip system. Note here that due to the symmetry of $\widetilde{\boldsymbol{S}}$, τ^{α} could equivalently be expressed as

$$\tau^{\alpha} = \widetilde{\boldsymbol{S}}:\mathrm{sym}(\widetilde{\boldsymbol{C}}^{e}\widetilde{\boldsymbol{Z}}^{\alpha}) = \widetilde{\boldsymbol{S}}:\widetilde{\boldsymbol{C}}^{e}\widetilde{\boldsymbol{Z}}^{\alpha} = \widetilde{\boldsymbol{C}}^{e}\widetilde{\boldsymbol{S}}:\widetilde{\boldsymbol{Z}}^{\alpha} \tag{2.25}$$

With these definitions, the dissipation inequality, Eq.(2.21), reduces to

$$\sum_{\alpha=1}^{N}\tau^{\alpha}\dot{\gamma}^{\alpha} - \sum_{\alpha=1}^{N}\kappa_{s}^{\alpha}\dot{\epsilon}_{s}^{\alpha} \geq 0 \tag{2.26}$$

where the first term represent the dissipation from plastic work due to slip processes (irreversible dislocation motion) and the second term gives the stored work due to the accumulation of dislocations. Note here that specific constitutive equations for $\widetilde{\boldsymbol{S}}$ and κ_{s}^{α} will follow from the assumed form for the free energy $\widetilde{\Psi}_{\mathrm{v}}$ using Eqs.(2.22)–(2.23).

2.3 The Crystal Plasticity Model.

The thermodynamic state of the material is assumed to be described by a quadratic form of the Helmoltz free energy on the elastic strains $(\widetilde{\boldsymbol{E}}^{e}, \epsilon_{s}^{\alpha})$, i.e.,

$$\widetilde{\Psi}_{\mathrm{v}} = \widehat{\widetilde{\Psi}}_{\mathrm{v}}(\widetilde{\boldsymbol{E}}^{e}, \epsilon_{s}^{\alpha}) = \frac{1}{2}\widetilde{\boldsymbol{E}}^{e}:\tilde{\mathbb{C}}^{e}:\widetilde{\boldsymbol{E}}^{e} + \frac{1}{2}\sum_{\alpha=1}^{N}\mu_{E}\,c_{\kappa}(\epsilon_{s}^{\alpha})^{2} \tag{2.27}$$

where $\tilde{\mathbb{C}}^{e}$ is the fourth order anisotropic crystal elasticity tensor, μ_{E} is an effective shear modulus, and c_{κ} is a material constant. Then, using Eqs.(2.22)–(2.23), we obtain the following constitutive equations

$$\widetilde{\boldsymbol{S}} = \tilde{\mathbb{C}}^{e}:\widetilde{\boldsymbol{E}}^{e}, \qquad \kappa_{s}^{\alpha} = \mu_{E}\,c_{\kappa}\epsilon_{s}^{\alpha} \tag{2.28}$$

To complement the model equations, one needs to prescribe the evolutions equation for the shearing rates γ^{α} (kinetic equation or flow rule) and lattice strains ϵ_{s}^{α} (hardening law). For now, we will denote these evolution equations as

$$\dot{\gamma}^{\alpha} = \Phi(\tau^{\alpha}, \kappa_{s}^{\alpha}), \qquad \dot{\epsilon}_{s}^{\alpha} = \Theta_{\epsilon}(\epsilon_{s}^{\alpha}, \dot{\gamma}^{\alpha}) \tag{2.29}$$

Then, the single crystal constitutive model expressed in the intermediate unloaded configuration $\widetilde{\mathcal{B}}$ can be formulated as

$$
\begin{aligned}
&\textit{Kinematics:} && \widetilde{\boldsymbol{D}} = \boldsymbol{V}^{eT}\boldsymbol{d}\boldsymbol{V}^{e} = \dot{\widetilde{\boldsymbol{E}}}^{e} + \widetilde{\boldsymbol{D}}^{\star} \\
& && \widetilde{\boldsymbol{W}} = \boldsymbol{V}^{eT}\boldsymbol{w}\boldsymbol{V}^{e} = \mathrm{skew}(\boldsymbol{V}^{eT}\dot{\boldsymbol{V}}^{e}) + \widetilde{\boldsymbol{W}}^{\star} \\
&\textit{Elasticity:} && \widetilde{\boldsymbol{S}} = \widetilde{\mathbb{C}}^{e} : \widetilde{\boldsymbol{E}}^{e} \\
&\textit{Plasticity:} && \widetilde{\boldsymbol{D}}^{\star} = \mathrm{sym}(\widetilde{\boldsymbol{C}}^{e}\widetilde{\boldsymbol{\Omega}}^{e}) + \sum_{\alpha=1}^{N} \dot{\gamma}^{\alpha}\mathrm{sym}(\widetilde{\boldsymbol{C}}^{e}\widetilde{\boldsymbol{Z}}^{\alpha}) \\
& && \widetilde{\boldsymbol{W}}^{\star} = \mathrm{skew}(\widetilde{\boldsymbol{C}}^{e}\widetilde{\boldsymbol{\Omega}}^{e}) + \sum_{\alpha=1}^{N} \dot{\gamma}^{\alpha}\mathrm{skew}(\widetilde{\boldsymbol{C}}^{e}\widetilde{\boldsymbol{Z}}^{\alpha}) \\
& && \dot{\gamma}^{\alpha} = \Phi(\tau^{\alpha}, \kappa_{s}^{\alpha}) \\
& && \tau^{\alpha} = \widetilde{\boldsymbol{S}} : \mathrm{sym}(\widetilde{\boldsymbol{C}}^{e}\widetilde{\boldsymbol{Z}}^{p}) = \widetilde{\boldsymbol{C}}^{e}\widetilde{\boldsymbol{S}} : \widetilde{\boldsymbol{Z}}^{\alpha} \\
& && \dot{\epsilon}_{s}^{\alpha} = \Theta_{\epsilon}(\epsilon_{s}^{\alpha}, \dot{\gamma}^{\alpha}), \qquad \kappa_{s}^{\alpha} = \mu_{E}\, c_{s}\epsilon_{s}^{\alpha}
\end{aligned}
\tag{2.30}
$$

2.4 Specialization to the Case of Small Elastic Strains.

Because the elastic strains in metals are orders of magnitude less than plastic strains in well-developed plastic flow, the above finite deformation crystal plasticity model is specialized here to the case of small applied elastic strains. For this purpose, we introduce the small elastic strain assumption for $\boldsymbol{V}^{e}$, i.e.,

$$
\boldsymbol{V}^{e} = \mathbf{1} + \boldsymbol{\epsilon}^{e}, \qquad \| \boldsymbol{\epsilon}^{e} \| \ll 1 \tag{2.31}
$$

In this case, configurations $\mathcal{B}$ and $\widetilde{\mathcal{B}}$ will differ by an infinitesimal amount. Then, using Eq.(2.31), we can write

$$
\dot{\boldsymbol{V}}^{e} = \dot{\boldsymbol{\epsilon}}^{e}, \qquad \boldsymbol{V}^{e-1} = \mathbf{1} - \boldsymbol{\epsilon}^{e} + \mathcal{O}(\| \boldsymbol{\epsilon}^{e} \|^{2}) \tag{2.32}
$$

With these approximations, many of the tensorial expressions given in the constitutive model (2.30) can be reduced. Specifically, the following relations can be derived after neglecting higher order terms $\mathcal{O}(\| \boldsymbol{\epsilon}^{e} \|^{2})$ and terms such as $(\bullet)\boldsymbol{\epsilon}^{e}$ and $\boldsymbol{\epsilon}^{e}(\bullet)$ in comparison to $(\bullet)$,

$$
\widetilde{\boldsymbol{D}} \approx \boldsymbol{d}, \qquad \widetilde{\boldsymbol{W}} \approx \boldsymbol{w}, \qquad \mathrm{skew}(\boldsymbol{V}^{eT}\dot{\boldsymbol{V}}^{e}) \approx \mathrm{skew}(\dot{\boldsymbol{\epsilon}}^{e}\boldsymbol{\epsilon}^{e}) \tag{2.33}
$$

$$
\widetilde{\boldsymbol{C}}^{e} \approx \mathbf{1}, \qquad \widetilde{\boldsymbol{E}}^{e} \approx \boldsymbol{\epsilon}^{e}, \qquad \widetilde{\boldsymbol{S}} \approx \boldsymbol{\tau} \tag{2.34}
$$

together with

$$\widetilde{\boldsymbol{D}}^{\star} \approx 2\mathrm{sym}(\boldsymbol{\epsilon}^e\widetilde{\boldsymbol{\Omega}}^e) + \sum_{\alpha=1}^{N}\dot{\gamma}^{\alpha}\mathrm{sym}(\widetilde{\boldsymbol{Z}}^{\alpha}) \tag{2.35}$$

$$\widetilde{\boldsymbol{W}}^{\star} \approx \widetilde{\boldsymbol{\Omega}}^e + \sum_{\alpha=1}^{N}\dot{\gamma}^{\alpha}\mathrm{skew}(\widetilde{\boldsymbol{Z}}^{\alpha}) \tag{2.36}$$

Once these approximations are introduced in the constitutive equations (2.30), the crystal plasticity model for small elastic strains can be formally simplified to

$$\begin{aligned}
&\textit{Kinematics:} && \boldsymbol{d} = \overset{\nabla}{\boldsymbol{\epsilon}}{}^e + \widetilde{\boldsymbol{D}}^p, \qquad \overset{\nabla}{\boldsymbol{\epsilon}}{}^e = \dot{\boldsymbol{\epsilon}}^e + \boldsymbol{\epsilon}^e\widetilde{\boldsymbol{\Omega}}^e - \widetilde{\boldsymbol{\Omega}}^e\boldsymbol{\epsilon}^e \\
& && \boldsymbol{w} = -\mathrm{skew}(\dot{\boldsymbol{\epsilon}}^e\boldsymbol{\epsilon}^e) + \widetilde{\boldsymbol{\Omega}}^e + \widetilde{\boldsymbol{W}}^p, \qquad \widetilde{\boldsymbol{\Omega}}^e = \dot{\boldsymbol{R}}^e\boldsymbol{R}^{eT} \\
&\textit{Elasticity:} && \boldsymbol{\tau} = \widetilde{\mathbb{C}}^e : \boldsymbol{\epsilon}^e \\
&\textit{Plasticity:} && \widetilde{\boldsymbol{D}}^p = \boldsymbol{R}^e\bar{\boldsymbol{D}}^p\boldsymbol{R}^{eT} = \sum_{\alpha=1}^{N}\dot{\gamma}^{\alpha}\mathrm{sym}(\widetilde{\boldsymbol{Z}}^{\alpha}) \\
& && \widetilde{\boldsymbol{W}}^p = \boldsymbol{R}^e\bar{\boldsymbol{W}}^p\boldsymbol{R}^{eT} = \sum_{\alpha=1}^{N}\dot{\gamma}^{\alpha}\mathrm{skew}(\widetilde{\boldsymbol{Z}}^{\alpha}) \\
& && \dot{\gamma}^{\alpha} = \Phi(\tau^{\alpha}, \kappa_s^{\alpha}) \\
& && \tau^{\alpha} = \boldsymbol{\tau} : \mathrm{sym}(\widetilde{\boldsymbol{Z}}^{\alpha}) = \boldsymbol{\tau} : \widetilde{\boldsymbol{Z}}^{\alpha} \\
& && \dot{\epsilon}_s^{\alpha} = \Theta_{\epsilon}(\epsilon_s^{\alpha}, \dot{\gamma}^{\alpha}), \qquad \kappa_s^{\alpha} = \mu_E\, c_s\epsilon_s^{\alpha}
\end{aligned} \tag{2.37}$$

where $\boldsymbol{\tau} = \det(\mathbf{1} + \boldsymbol{\epsilon}^e)\boldsymbol{\sigma}$. As mentioned before, when $\boldsymbol{\epsilon}^e = \mathbf{0}$ (i.e. when $\boldsymbol{V}^e = \mathbf{1}$) the above constitutive equations will model the response of a rigid–viscoplastic crystal. It is noted here that, from a mathematical point of view, the above model can be seen as a set of coupled first order ordinary differential equations for the kinematic variables ($\boldsymbol{\epsilon}^e$, $\boldsymbol{R}^e$, ϵ_s^{α}), or equivalently for the set ($\boldsymbol{\tau}$, $\boldsymbol{R}^e$, κ_s^{α}). As such, the corresponding numerical integration will be devised to solve for either of these variable sets.

Remark 2. In many applications of crystal plasticity theories, one needs to relate the response of individual crystals in an aggregate (or polycrystal) to the macroscopic behavior of the associated continuum (material) point. The relation between both responses can be obtained using a particular mean field hypothesis or partitioning rule. Specifically, microstructural (crystal) quantities such as ($\boldsymbol{d}$, $\boldsymbol{w}$, $\boldsymbol{\sigma}$) need be linked to their corresponding macroscopic counterparts ($\boldsymbol{D}_M$, $\boldsymbol{W}_M$, $\boldsymbol{\Sigma}_M$). In this work, where needed, we use an extended Taylor hypothesis [Asaro & Needleman, 1985], i.e.,

$$\boldsymbol{D}_M = \boldsymbol{d}, \qquad \boldsymbol{W}_M = \boldsymbol{w}, \qquad \boldsymbol{\Sigma}_M = \langle\boldsymbol{\sigma}\rangle \tag{2.38}$$

where the symbol $\langle(\bullet)\rangle$ denoted the volume average of $(\bullet)$ over all crystal orientations representing the aggregate texture. It is important to note that for crystals exhibiting markedly anisotropic yield surfaces, such as HCP crystals, equal partitioning of the deformation among all crystals in an aggregate, Eqs.$(2.38)_{1-2}$, may lead to physically unrealistic results [Kocks, *et al.*, 1998]. In this case, more general partitioning rules should be used. However, since Taylor hypothesis is mainly used here to validate the numerical implementation of the model (2.37) and no predictions of experimental results for HCP metals are sought, we will still use Eqs.(2.38) for computing the average behavior of HCP crystal aggregates.

2.5 Specific Constitutive Equations.

2.5.1 Slip System Kinetics (Flow Rule).

A physically-based description of the kinetics of slip relies on the theory of thermally activated dislocation motion [Kocks, *et al.*, 1975] [Meyers, *et al.*, 2002]. In this theory, it is assumed that the resolved shear stress on the α–slip system can be additively decomposed as $|\tau^\alpha| = \tau_a^\alpha + \tau_\star^\alpha$, where τ_a^α and $\tau_\star^\alpha$ are the applied shear stresses needed to overcome the athermal (long-range) and thermal (short-range) barriers to dislocation motion, respectively. Similarly, the resistance to slip (slip system strength or hardness) is partition as $\kappa_s^\alpha = \kappa_{s,\,a}^\alpha + \kappa_{s,\,\star}^\alpha$, where $\kappa_{s,\,a}^\alpha$ and $\kappa_{s,\,\star^\alpha}$ represent, respectively, the resistance of the athermal and thermal obstacles to dislocations gliding on the α–slip plane. Following [Kothary & Anand, 1998], we assume that the athermal components are the same, i.e., $\tau_a^\alpha = \kappa_{s,\,a}^\alpha$, while the thermal components, $\tau_\star^\alpha$ and $\kappa_{s,\,\star}^\alpha$ with $0 \leq \tau_\star^\alpha \leq \kappa_{s,\,\star}^\alpha$, define the slip system plastic shear strain rate as

$$\dot{\gamma}^\alpha = \dot{\gamma}_0 \exp\left\{-\frac{\Delta F}{k\theta}\left[1-\left(\frac{\tau_\star^\alpha}{\kappa_{s,\,\star}^\alpha}\right)^p\right]^q\right\}\operatorname{sign}(\tau^\alpha) \tag{2.39}$$

where k is the Boltzmann constant, θ is temperature, $\dot{\gamma}_0$ is a reference shear strain rate typically in the range $(10^6 - 10^8)\,s^{-1}$, and the parameters p and q, which control the shape of the glide resistance profile (thermal obstacles), adopt values in the ranges $0 \leq p \leq 1$ and $1 \leq q \leq 2$. In the above equation, ΔF is the activation free energy required to overcome the obstacles to slip without the aid of an applied shear stress and usually lies in the range $\Delta F = (0.05 - 2)\mu_E b^3$ [Frost & Ashby, 1982]. The parameters $\dot{\gamma}_0$ and ΔF are taken to be the same for all slip systems. Note here that $\tau_\star^\alpha = |\tau^\alpha| - \kappa_a^\alpha$, and hence, $\tau_\star^\alpha$ can be interpreted as an effective shear stress acting on the α–slip system.

For the case of non-zero plastic shearing rates, we can invert Eq.(2.39) to obtain

$$\tau_\star^\alpha = S(|\dot{\gamma}^\alpha|,\theta)\kappa_{s,\,\star}^\alpha \quad \rightarrow \quad |\tau^\alpha| = \kappa_a^\alpha + S(|\dot{\gamma}^\alpha|,\theta)\,\kappa_{s,\,\star}^\alpha \tag{2.40}$$

where the factor $S(|\dot{\gamma}^\alpha|,\theta) \leq 1$ is given by

$$S(|\dot{\gamma}^\alpha|,\theta) = \left[1-\left(\frac{\theta}{\theta_c}\right)^{1/q}\right]^{1/p}, \qquad \theta_c = \frac{\Delta F}{k\ln(\dot{\gamma}_0/|\dot{\gamma}^\alpha|)} \tag{2.41}$$

At a given strain rate $\dot{\gamma}^\alpha$, the temperature θ_c sets the limit of applicability of the thermal–activation model for slip kinetics. That is, for temperatures above θ_c, there is enough thermal energy for the barriers to be overcome by thermal activation alone, without the aid of an applied stress. Note that at $\theta = 0$, we get $S = 1$ ($\tau^\alpha_\star = \kappa^\alpha_{s,\star}$), and at $\theta = \theta_c$ we have $S = 0$ ($\tau^\alpha_\star = 0$).

An alternative description for the kinetics of slip is based on the well–known power law model given by

$$\dot{\gamma}^\alpha = \dot{\gamma}_0 \left[\frac{|\tau^\alpha|}{\kappa^\alpha_s}\right]^{1/m} \text{sign}(\tau^\alpha) \tag{2.42}$$

This empirical relationship has been widely used to represent most of the experimental results in the thermally activated regime. To establish a connection between the above power–law–based kinetics and the physics-based kinetics, Eq.(2.39), one could derive an expression for a rate sensitivity parameter m using Eq.$(2.40)_2$ to obtain [Kothary & Anand, 1998]

$$m = \frac{\partial \ln|\tau^\alpha|}{\partial \ln|\dot{\gamma}^\alpha|}\Big|_{\kappa^\alpha_s,\theta} = \frac{k\theta}{\Delta F}\,\frac{1}{pq}\left(\frac{\theta}{\theta_c}\right)^{1/q-1}\left[1-\left(\frac{\theta}{\theta_c}\right)^{1/q}\right]^{-1} \tag{2.43}$$

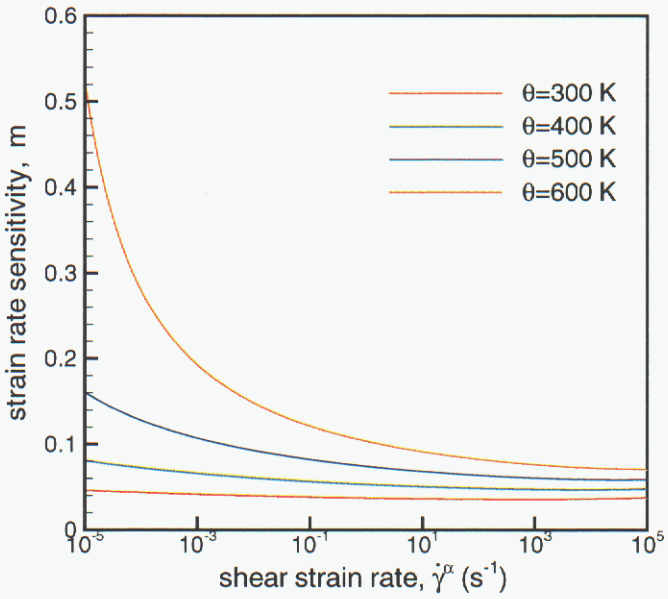

Figure 2.2: Typical variation of the strain–rate sensitivity parameter m with strain rate and temperature, computed from Eq.(2.43) with the parameter values: $\Delta F = 2.5 \times 10^{-19}\, J$, $\dot{\gamma}_0 = 10^7\, s^{-1}$, $p = 3/4$, $q = 4/3$ ($k = 1.3807 \times 10^{-23}\, J\, K^{-1}$).

Using typical values for the parameters, we plot in Fig. 2.2 the variation of m against strain rate at fixed representative temperatures. It is observed from this figure that the

power law relation requires the use of a "variable" (rate– and temperature–dependent) m in order to capture the flow behavior of metals under a wide range of temperatures and strain rates. Because the simulations presented in this document are limited to low strain rates and isothermal conditions (room temperature), the power law approximation with a fixed m will still be used as a model for the kinetics of slip. Future applications of the model framework (2.37) to a wider range of loading conditions will consider the physically-based description given by Eq.(2.39).

2.5.2 Slip System Strength (Hardening Rule).

To formulate a dislocation-based hardening law, we rely on the evolution equation for dislocation density ρ_s^α proposed by [Cocks & Mecking, 1979]. This equation assumes that hardening is controlled by the competition of storage and annihilation of (statistically stored) dislocations. The (athermal) storage rate is described by a mean free path Λ^α ($\propto 1/\sqrt{\rho_s^\alpha}$) that the dislocations travel before being immobilized, while the annihilation (dynamic recovery) follows a first order kinetics, i.e., it is linear in ρ_s^α. Hence,

$$\dot{\rho}_s^\alpha = \Big(\frac{c_1}{\Lambda^\alpha} - c_2\rho_s^\alpha\Big)|\dot{\gamma}^\alpha|, \qquad \Lambda^\alpha \propto \frac{1}{\sqrt{\rho_s^\alpha}} \tag{2.44}$$

where c_1 and c_2 are constants, with $c_2 = \hat{c}_2(|\dot{\gamma}^\alpha|, \theta)$ (dynamic recovery is thermally activated). The above equation can be transformed to an evolution equation in the internal elastic strain ϵ_s^α using $\epsilon_s^\alpha = b\sqrt{\rho_s^\alpha}$, and relating the constants c_1 and c_2 to meaningful physical quantities as $c_1 = 2h_0^\alpha/(c_\kappa \mu_E b)$ and $c_2 = 2h_0^\alpha/(c_\kappa \mu_E \epsilon_{s,S}^\alpha)$ [Acharya & Beaudoin, 2000]. Here, h_0^α is the initial hardening rate due to dislocation accumulation, and $\epsilon_{s,S}$ is a saturation internal strain which, in general, is a function of strain rate and temperature. Then Eq.(2.44) can be written as

$$\dot{\epsilon}_s^\alpha = \Theta_\epsilon(\epsilon_s^\alpha, \dot{\gamma}^\alpha), \qquad \Theta_\epsilon(\epsilon_s^\alpha, \dot{\gamma}^\alpha) = \frac{h_0^\alpha}{c_\kappa \mu_E}\Big(1 - \frac{\epsilon_s^\alpha}{\epsilon_{s,S}^\alpha}\Big)|\dot{\gamma}^\alpha| \tag{2.45}$$

In fact, in the open literature the above relationship is usually given in terms of the slip system strength κ_s^α, expression that can be obtained using Eq.(2.45) together with Eq.(2.27). To account for the initial strength $\kappa_{s,0}^\alpha$ explicitly, we slightly modified Eq.(2.27) to $\kappa_s^\alpha = \kappa_{s,0}^\alpha + c_\kappa \mu_E \epsilon_s^\alpha$ [Mecking & Cocks, 1981] and write the evolution equation for κ_s^α as

$$\dot{\kappa}_s^\alpha = h^\alpha|\dot{\gamma}^\alpha|, \qquad h^\alpha = h_0^\alpha\Big(1 - \frac{\kappa_s^\alpha - \kappa_{s,0}^\alpha}{\kappa_{s,S}^\alpha - \kappa_{s,0}^\alpha}\Big) \tag{2.46}$$

Although extensions of the above equation to include latent hardening effects and more complex hardening functions h^α are possible [Balasubramanian & Anand, 2002], [Kok, *et al.*, 2002], in this work we just use a simplified version of Eq.(2.46) obtained by assuming that all slip systems harden at the same rate ($\kappa_s^\alpha \to \kappa_s$, i.e., only one hardness variable needed to represent the crystal strength), and hence replace Eq.(2.46) by

$$\dot{\kappa}_s = \Theta_\kappa(\kappa_s, \dot{\gamma}^\alpha), \qquad \Theta_\kappa(\kappa_s, \dot{\gamma}^\alpha) = h_0\Big(\frac{\kappa_{s,S} - \kappa_s}{\kappa_{s,S} - \kappa_{s,0}}\Big)\sum_{\alpha=1}^{N}|\dot{\gamma}^\alpha| \tag{2.47}$$

where the saturation strength $\kappa_{s,S}$ is given by [Follansbee & Cocks, 1988]

$$\kappa_{s,S} = \hat{\kappa}_{s,S}(|\dot{\gamma}^{\alpha}|, \theta) = \kappa_{s,S0} \left[\frac{\sum_{\alpha} |\dot{\gamma}^{\alpha}|}{\dot{\gamma}_{S0}} \right]^{k\theta/\mu_E b^3 A} \tag{2.48}$$

with $\kappa_{s,S0}, \dot{\gamma}_{S0}$, and A being material parameters. As mentioned above, the applications presented in this work will be limited to isothermal cases (room temperature), and hence the exponent in Eq.(2.48) will be simply replaced by a constant m'.

3. Numerical Implementation

In a numerical setting, classical crystal plasticity has been used in combination with the finite element method to provide numerical solutions to boundary value problems involving anisotropic material behavior. In this context, crystal plasticity provides the material properties at each computational point in the finite element discretization. In general, two types of applications are distinguished here, depending on whether the material properties at the computational point represents the mechanical response of an aggregate of crystals or just that of a single crystal. In the literature, these applications have been termed large and small scale applications [Kocks, *et al.*, 1998]. Typically the former has been used to study the effect of plastic anisotropy (texture) on the material response at the macroscopic level during materials processing such as rolling and sheet forming [Beaudoin, *et al.*, 1994], while the latter (also called direct numerical simulation–DNS– of polycrystals) has been applied to investigate heterogeneous deformation patterns of both single crystals and aggregate of crystals to get a better insight into the plastic response of polycrystals [Sarma & Dawson, 1996]. Detailed features of each type of application have been described in [Kocks, *et al.*, 1998].

In this work, our interest is the use of crystal plasticity models to better understand materials with considerable heterogeneity of deformation over the dimension of an aggregate of crystals (small scale applications). As mentioned in [Kocks, *et al.*, 1998], a particular feature of this mesoscale approach, which is illustrated in Fig. 3.1, is that finite elements discretize the crystals (grains) and balance laws are applied to the level of individual crystals. The numerical solution to the field equations then renders the partition of the deformation among the crystals (mean field hypothesis such as Taylor model are not needed in this approach). With the applied deformation on each crystal known, the crystal state is evolved by numerically integrating the crystal constitutive equations. The single crystal state then defines directly the anisotropic material behavior at each computational point of the finite element model.

In this section we develop an implicit numerical integration procedure for the proposed crystal constitutive model, Eqs.(2.37). We also derive an "approximate" algorithmic material moduli for use in implicit finite element simulations. The integration scheme and corresponding algorithmic moduli are implemented in both a material point simulation code and a commercial finite element code and validated in the next section by solving a number of problems.

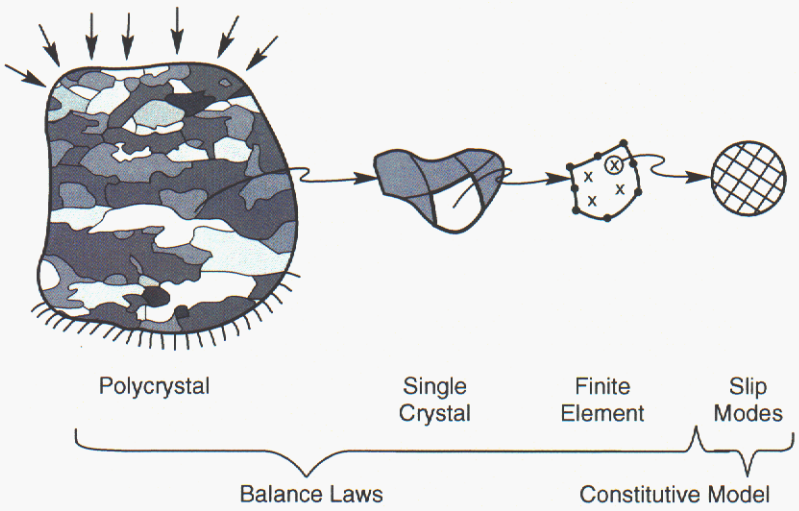

Figure 3.1: The combination of crystal plasticity theory and the finite element method to study the behavior of crystal aggregates: small scale applications or direct numerical simulation–DNS– of polycrystals (after [Kocks, *et al.*, 1998]).

3.1 General Remarks.

Consider the orthogonal basis $\{\boldsymbol{e}_i\}_{i=1,3}$ and $\{\boldsymbol{e}^c_A\}_{A=1,3}$, aligned with the fixed (sample) frame and crystal lattice, respectively. These basis can be related by the rotation $\boldsymbol{e}_i = \boldsymbol{C}\cdot\boldsymbol{e}^c_A$, where $\boldsymbol{C} \in SO(3)$. In terms of the Euler angles $(\varphi_1, \phi, \varphi_2)$ (Cocks convention [Kocks, *et al.*, 1998]), the rotation tensor $\boldsymbol{C}$ will have the matrix representation

$$[C]=\begin{bmatrix} \cos\varphi_1\cos\varphi_2-\sin\varphi_1\cos\phi\sin\varphi_2 & -\cos\varphi_1\sin\varphi_2-\sin\varphi_1\cos\phi\cos\varphi_2 & \sin\varphi_1\sin\phi \\ \sin\varphi_1\cos\varphi_2+\cos\varphi_1\cos\phi\sin\varphi_2 & -\sin\varphi_1\sin\varphi_2+\cos\varphi_1\cos\phi\cos\varphi_2 & -\cos\varphi_1\sin\phi \\ \sin\varphi_2\sin\phi & \cos\varphi_2\sin\phi & \cos\phi \end{bmatrix} \tag{3.1}$$

with $0\leq\varphi_1\leq 2\pi,\quad 0\leq\phi\leq\pi,\quad 0\leq\varphi_2\leq 2\pi$. In a numerical setting, this rotation matrix is used to transform to the sample coordinate system in configuration $\widetilde{\mathcal{B}}$, the time-independent orthonormal slip system vectors $(\boldsymbol{s}^\alpha_0,\ \boldsymbol{m}^\alpha_0)$ and the fourth order tensor of elastic moduli $\mathbb{C}^e_0$ both of which referred to the lattice axis,

$$\widetilde{\boldsymbol{s}}^\alpha = \boldsymbol{C}\,\boldsymbol{s}^\alpha_0,\quad \widetilde{\boldsymbol{m}}^\alpha = \boldsymbol{C}\,\boldsymbol{m}^\alpha_0 \tag{3.2}$$

$$\widetilde{\mathbb{C}}^e = (\boldsymbol{C}\underline{\otimes}\boldsymbol{C}) : \mathbb{C}^e_0 : (\boldsymbol{C}\underline{\otimes}\boldsymbol{C})^T \tag{3.3}$$

where $(\boldsymbol{C}\underline{\otimes}\boldsymbol{C})_{ijAB} = C_{iA}C_{jB}$. The initial orientation $\boldsymbol{C}_0$ $(\varphi_{10}, \phi_0, \varphi_{20})$ is prescribed as part of the crystal initial state, and it is numerically updated during a given deformation history using $\boldsymbol{C} = \boldsymbol{R}^e\boldsymbol{C}_0$, where $\boldsymbol{R}^e$ is the rotation tensor from the polar decomposition of $\boldsymbol{F}^e$, as represented in the kinematics Eq.(2.1) and whose evolution equation is given by Eq.$(2.37)_2$. Note here that the orthonormal slip system vectors $(\bar{\boldsymbol{s}}^\alpha,\ \bar{\boldsymbol{m}}^\alpha)$ in $\bar{\mathcal{B}}$, referred to the sample

reference frame, are related to the vectors $(\boldsymbol{s}_0^\alpha,\ \boldsymbol{m}_0^\alpha)$ by $\bar{\boldsymbol{s}}^\alpha = \boldsymbol{C}_0\boldsymbol{s}_0^\alpha$, $\bar{\boldsymbol{m}}^\alpha = \boldsymbol{C}_0\boldsymbol{m}_0^\alpha$. Hence, $\bar{\boldsymbol{Z}}^\alpha = \boldsymbol{C}_0\boldsymbol{Z}_0^\alpha\boldsymbol{C}_0^T$ and $\widetilde{\boldsymbol{Z}}^\alpha = \boldsymbol{C}\boldsymbol{Z}_0^\alpha\boldsymbol{C}^T$, where $\boldsymbol{Z}_0^\alpha = \boldsymbol{s}_0^\alpha \otimes \boldsymbol{m}_0^\alpha$.

The orthonormal slip system vectors $(\boldsymbol{s}_0^\alpha, \boldsymbol{m}_0^\alpha)$ will have values according to the type of crystalline lattice (e.g., cubic, hexagonal). For cubic crystals, only the $12\{111\}\langle 110\rangle$ slip systems are considered for FCC metals, whereas for BCC metals, the $12\{110\}\langle 111\rangle$ and the $12\{112\}\langle 111\rangle$ may be included. In the case of HCP crystals, slip is typically assumed on the $3(0001)\langle 11\bar{2}0\rangle$ basal, the $3\{10\bar{1}0\}\langle 11\bar{2}0\rangle$ prismatic and the $12\{10\bar{1}1\}\langle 11\bar{2}3\rangle$ pyramidal slip systems. On the other hand, the number of constants needed to specify the anisotropic elasticity tensor, $\mathbb{C}_0^e$, will also depend on the crystal structure. In this respect, consider Voight (vector) notation for the stress and strain tensors, i.e.,

$$\boldsymbol{\tau} \rightarrow \{\tau\} = \{\tau_{11} \quad \tau_{22} \quad \tau_{33} \quad \tau_{12} \quad \tau_{13} \quad \tau_{23}\}^T \tag{3.4}$$

$$\boldsymbol{\epsilon}^e \rightarrow \{\epsilon^e\} = \{\epsilon_{11}^e \quad \epsilon_{22}^e \quad \epsilon_{33}^e \quad 2\epsilon_{12}^e \quad 2\epsilon_{13}^e \quad 2\epsilon_{23}^e\}^T \tag{3.5}$$

Using this notation, one can write the elasticity law in matrix form as

$$\boldsymbol{\tau} = \widetilde{\mathbb{C}}^e : \boldsymbol{\epsilon}^e \qquad \rightarrow \qquad \{\tau\} = [\mathbb{C}^e]\{\epsilon^e\} \tag{3.6}$$

where $[\mathbb{C}^e]$ is the elasticity matrix in the sample coordinate system. With respect to the crystal axis (subscript 0), this matrix is fully specified by

$$[\mathbb{C}^e]_0 = \begin{bmatrix} C_{11} & C_{12} & C_{12} & & & & \\ C_{12} & C_{11} & C_{12} & & & & \\ C_{12} & C_{12} & C_{11} & & & & \\ & & & C_{44} & & & \\ & & & & C_{44} & & \\ & & & & & C_{44} & \end{bmatrix}, \tag{3.7}$$

for the case of cubic crystals (3 material constants), and by

$$[\mathbb{C}^e]_0 = \begin{bmatrix} C_{11} & C_{12} & C_{13} & & & & \\ C_{12} & C_{11} & C_{13} & & & & \\ C_{13} & C_{13} & C_{33} & & & & \\ & & & C_{55} & & & \\ & & & & C_{44} & & \\ & & & & & C_{44} & \end{bmatrix} \tag{3.8}$$

with $C_{55} = \frac{1}{2}(C_{11} - C_{12})$, for the case of HCP crystals (5 material constants).

3.2 Anisotropic Crystal Elasticity.

For computational convenience, the elastic law given by Eq.(2.37)$_3$ is written as

$$\mathrm{dev}\boldsymbol{\tau} = \widetilde{\mathbb{C}}_d^e : \mathrm{dev}\boldsymbol{\epsilon}^e + \widetilde{\boldsymbol{H}}^e \epsilon_{kk}^e \tag{3.9}$$

$$p_\tau = \widetilde{\boldsymbol{H}}^{eT} : \mathrm{dev}\boldsymbol{\epsilon}^e + \widetilde{M}^e \epsilon_{kk}^e \tag{3.10}$$

where $\boldsymbol{\tau} = \mathrm{dev}\boldsymbol{\tau} + p_\tau \tilde{\mathbf{1}}$, with $\mathrm{dev}\boldsymbol{\tau}$ and p_τ being the deviatoric and spherical (hydrostatic) parts of $\boldsymbol{\tau}$, respectively. In Eqs.(3.9)–(3.10) we have defined

$$\widetilde{\mathbb{C}}_d^e = \widetilde{\mathbb{P}}_d : \widetilde{\mathbb{C}}^e : \widetilde{\mathbb{P}}_d, \qquad \widetilde{\boldsymbol{H}}^e = \frac{1}{3}\widetilde{\mathbb{P}}_d : \widetilde{\mathbb{C}}^e : \tilde{\mathbf{1}}, \qquad \widetilde{M}^e = \frac{1}{9}\tilde{\mathbf{1}} : \widetilde{\mathbb{C}}^e : \tilde{\mathbf{1}} \tag{3.11}$$

where $\widetilde{\mathbb{C}}_d^e$ is the fourth order deviatoric elasticity tensor, $\widetilde{\boldsymbol{H}}^e$ is the second order deviatoric–isochoric elastic coupling tensor, and $\widetilde{M}^e$ is the elastic volumetric coefficient. Besides, $\widetilde{\mathbb{P}}_d = \widetilde{\mathbb{I}} - \frac{1}{3}\tilde{\mathbf{1}} \otimes \tilde{\mathbf{1}}$ is the fourth order deviatoric projection tensor, with $\widetilde{\mathbb{I}}$ and $\tilde{\mathbf{1}}$ being the fourth order and second order unit tensors. Note here that

$$\widetilde{\mathbb{C}}_d^e = (\boldsymbol{C} \underline{\otimes} \boldsymbol{C}) : \mathbb{C}_{d0}^e : (\boldsymbol{C} \underline{\otimes} \boldsymbol{C})^T, \qquad \widetilde{\boldsymbol{H}}^e = \boldsymbol{C}\boldsymbol{H}_0^e\boldsymbol{C}^T, \qquad \widetilde{M}^e = M_0^e \tag{3.12}$$

with $\mathbb{C}_{d0}^e$, $\boldsymbol{H}_0^e$, and M_0^e being referred to the crystal axis. For the vector representation [Marin & Dawson, 1998]

$$\mathrm{dev}\boldsymbol{\tau} \rightarrow \{\tau'\} = \left\{\frac{1}{\sqrt{2}}(\tau_{11}' - \tau_{22}') \quad \sqrt{\frac{3}{2}}\tau_{33}' \quad \sqrt{2}\tau_{12}' \quad \sqrt{2}\tau_{13}' \quad \sqrt{2}\tau_{23}'\right\}^T, \tag{3.13}$$

$$\mathrm{dev}\boldsymbol{\epsilon}^e \rightarrow \{\epsilon^{e\prime}\} = \left\{\frac{1}{\sqrt{2}}(\epsilon_{11}^{e\prime} - \epsilon_{22}^{e\prime}) \quad \sqrt{\frac{3}{2}}\epsilon_{33}^{e\prime} \quad \sqrt{2}\epsilon_{12}^{e\prime} \quad \sqrt{2}\epsilon_{13}^{e\prime} \quad \sqrt{2}\epsilon_{23}^{e\prime}\right\}^T, \tag{3.14}$$

Eqs.(3.9)–(3.10) can be written in matrix notation as

$$\{\tau'\} = [\widetilde{\mathbb{C}}_d^e]\{\epsilon^{e\prime}\} + \{\widetilde{H}^e\}\epsilon_{kk}^e \tag{3.15}$$

$$p_\tau = \{\widetilde{H}^e\}^T\{\epsilon^{e\prime}\} + \widetilde{M}^e\epsilon_{kk}^e \tag{3.16}$$

where, with respect to the crystal axis, the quantities $[\mathbb{C}_d^e]_0$, $\{H^e\}_0$ and M_0^e can be expressed as

$$[\mathbb{C}_d^e]_0 = \begin{bmatrix} C_{11}\text{–}C_{12} & & & & & \\ & C_{11}\text{–}C_{12} & & & & \\ & & 2C_{44} & & & \\ & & & 2C_{44} & & \\ & & & & 2C_{44} & \end{bmatrix} \tag{3.17}$$

$$\{H^e\}_0 = \{0 \quad 0 \quad 0 \quad 0 \quad 0\}^T \tag{3.18}$$

$$M_0^e = \frac{1}{3}(C_{11} + 2C_{12}) \tag{3.19}$$

for cubic crystals, while they can be written as

$$[\mathbb{C}_d^e]_0 = \begin{bmatrix} C_{11}-C_{12} & & & & & \\ & \frac{1}{3}(C_{11}-C_{12}-4C_{13}+2C_{33}) & & & & \\ & & C_{11}-C_{12} & & & \\ & & & 2C_{44} & & \\ & & & & 2C_{44} & \end{bmatrix} \tag{3.20}$$

$$\{H^e\}_0 = -\frac{\sqrt{6}}{9}\{0 \quad C_{11} + C_{22} - C_{13} - C_{33} \quad 0 \quad 0 \quad 0\}^T \tag{3.21}$$

$$M_0^e = \frac{1}{9}(2C_{11} + 2C_{12} + 4C_{13} + C_{33}) \tag{3.22}$$

for HCP crystals. Note that the matrix $[\mathbb{C}_d^e]_0$ is diagonal, a convenient form for numerical operations.

Remark 3. Effective elastic properties can be defined for cubic and hexagonal crystals in terms of the elastic constants appearing in $[\mathbb{C}^e]_0$. Denote K_E and μ_E as the effective elastic bulk and shear modulus, respectively. For cubic crystals they can be defined as

$$K_E = M_0^e = \frac{1}{3}(C_{11}+2C_{12}), \qquad \mu_E = \frac{1}{5}(C_{11}-C_{12}+3C_{13}), \tag{3.23}$$

while for hexagonal crystals they are determined as

$$K_E = \frac{(C_{11}+C_{12})C_{33}-2C_{13}^2}{C_{11}+C_{12}-4C_{13}+2C_{33}}, \qquad \mu_E = \frac{1}{30}(7C_{11}-5C_{12}-4C_{13}+2C_{33}+12C_{44}) \tag{3.24}$$

In this last case, if $C_{11} + C_{12} = C_{13} + C_{33}$, then

$$K_E = \frac{1}{3}(2C_{13} + C_{33}) = M_0^e \tag{3.25}$$

3.3 Constitutive Integration Scheme.

The crystal constitutive model, Eqs.(2.37), can be considered as a set of coupled first order ordinary differential equations for the variables ($\boldsymbol{\epsilon}^e$, $\boldsymbol{R}^e$, ϵ_s^α), or equivalently for ($\boldsymbol{\tau}$, $\boldsymbol{R}^e$, κ_s^α). The time integration of these evolutionary equations is carried out in the sample axis

and proceeds by discretizing the deformation history in time and numerically integrating the equations over each time step. For this purpose, we consider the configurations of the body at time t_n and t_{n+1} with $t_{n+1} = t_n + \Delta t$. Accordingly, variables evaluated at t_n and t_{n+1} will be denoted with the subscripts n and $n+1$ respectively. This integration scheme is developed assuming (i) that the crystal deformation represented by $\boldsymbol{l}_{n+1}$ (or $\boldsymbol{d}_{n+1}$ and $\boldsymbol{w}_{n+1}$) is given, (ii) that the variables ($\boldsymbol{\epsilon}^e_n$, $\boldsymbol{R}^e_n$, $\epsilon^\alpha_{s,n}$) or ($\boldsymbol{\tau}_n$, $\boldsymbol{R}^e_n$, $\kappa^\alpha_{s,n}$) are known, and (iii) that the time-independent slip system vectors ($\boldsymbol{s}^\alpha_0$, $\boldsymbol{m}^\alpha_0$), the elasticity tensor $\mathbb{C}^e_0$, the initial crystal orientation $\boldsymbol{C}_0$ (texture), and the plasticity material parameters (flow rule and hardening law) are input. The integration of the model will then give the updated values ($\boldsymbol{\epsilon}^e_{n+1}$, $\boldsymbol{R}^e_{n+1}$, $\epsilon^\alpha_{s,n+1}$) or ($\boldsymbol{\tau}_{n+1}$, $\boldsymbol{R}^e_{n+1}$, $\kappa^\alpha_{s,n+1}$).

This numerical integration proceeds as follows. The kinematics given by Eq.(2.37)$_1$ and written as

$$\overset{\nabla}{\boldsymbol{\epsilon}}{}^e = \boldsymbol{R}^e \left[\frac{\partial}{\partial t} (\boldsymbol{R}^{eT} \boldsymbol{\epsilon}^e \boldsymbol{R}^e) \right] \boldsymbol{R}^{eT} = \boldsymbol{d} - \widetilde{\boldsymbol{D}}^p \tag{3.26}$$

is integrated using a backward Euler scheme, resulting in

$$\boldsymbol{R}^{eT}_{n+1} \boldsymbol{\epsilon}^e_{n+1} \boldsymbol{R}^e_{n+1} = \boldsymbol{R}^{eT}_n \boldsymbol{\epsilon}^e_n \boldsymbol{R}^e_n + \Delta t \boldsymbol{R}^{eT}_{n+1} (\boldsymbol{d}_{n+1} - \widetilde{\boldsymbol{D}}^p_{n+1}) \boldsymbol{R}^e_{n+1} \tag{3.27}$$

or

$$\boldsymbol{\epsilon}^e_{n+1} = \underbrace{\boldsymbol{R}^e_{n+1} \boldsymbol{R}^{eT}_n}_{\Delta \boldsymbol{R}^e} \boldsymbol{\epsilon}^e_n \underbrace{\boldsymbol{R}^e_n \boldsymbol{R}^{eT}_{n+1}}_{\Delta \boldsymbol{R}^{eT}} + \Delta t (\boldsymbol{d}_{n+1} - \widetilde{\boldsymbol{D}}^p_{n+1}) \tag{3.28}$$

where $\Delta \boldsymbol{R}^e$ is the incremental elastic rotation tensor. From Eq.(2.37)$_4$, the plastic strain rate $\widetilde{\boldsymbol{D}}^p_{n+1}$ can be expressed as

$$\begin{aligned} \widetilde{\boldsymbol{D}}^p_{n+1} = \boldsymbol{R}^e_{n+1} \bar{\boldsymbol{D}}^p_{n+1} \boldsymbol{R}^{eT}_{n+1} &= \boldsymbol{R}^e_{n+1} \mathrm{sym} \Big(\sum_{\alpha=1}^N \dot{\gamma}^\alpha_{n+1} \bar{\boldsymbol{s}}^\alpha \otimes \bar{\boldsymbol{m}}^\alpha \Big) \boldsymbol{R}^{eT}_{n+1} \\ &= \sum_{\alpha=1}^N \dot{\gamma}^\alpha_{n+1} \mathrm{sym} \Big(\underbrace{\boldsymbol{R}^e_{n+1} \boldsymbol{C}_0}_{\boldsymbol{C}_{n+1}} \boldsymbol{s}^\alpha_0 \otimes \underbrace{\boldsymbol{R}^e_{n+1} \boldsymbol{C}_0}_{\boldsymbol{C}_{n+1}} \boldsymbol{m}^\alpha_0 \Big) \\ &= \sum_{\alpha=1}^N \dot{\gamma}^\alpha_{n+1} \mathrm{sym} \Big(\widetilde{\boldsymbol{s}}^\alpha_{n+1} \otimes \widetilde{\boldsymbol{m}}^\alpha_{n+1} \Big) = \sum_{\alpha=1}^N \dot{\gamma}^\alpha_{n+1} \mathrm{sym} \widetilde{\boldsymbol{Z}}^\alpha_{n+1} \end{aligned} \tag{3.29}$$

where, from Eqs.(2.37)$_{5-6}$, $\dot{\gamma}^\alpha_{n+1} = \widehat{\dot{\gamma}}^\alpha(\boldsymbol{\tau}_{n+1}, \kappa^\alpha_{n+1})$. In these equations, $\widetilde{\boldsymbol{s}}^\alpha_{n+1} = \boldsymbol{C}_{n+1} \boldsymbol{s}^\alpha_0$ and $\widetilde{\boldsymbol{m}}^\alpha_{n+1} = \boldsymbol{C}_{n+1} \boldsymbol{m}^\alpha_0$ are the slip system vectors in configuration $\widetilde{\mathcal{B}}_{n+1}$. As mentioned before, the rotation matrix $\boldsymbol{C}_{n+1} = \boldsymbol{R}^e_{n+1} \boldsymbol{C}_0$ updates the crystal orientation (Euler angles) and it is used to transform the tensors $\mathbb{C}^e_0$ and $\boldsymbol{H}^e_0$ to configuration $\widetilde{\mathcal{B}}_{n+1}$,

$$\widetilde{\mathbb{C}}^e_{n+1} = (\boldsymbol{C}_{n+1} \underline{\otimes} \boldsymbol{C}_{n+1}) : \mathbb{C}^e_0 : (\boldsymbol{C}_{n+1} \underline{\otimes} \boldsymbol{C}_{n+1})^T, \qquad \widetilde{\boldsymbol{H}}^e_{n+1} = \boldsymbol{C}_{n+1} \boldsymbol{H}^e_0 \boldsymbol{C}^T_{n+1}. \tag{3.30}$$

Denoting $\widetilde{\boldsymbol{P}}^{\alpha}_{n+1} = \mathrm{sym}(\widetilde{\boldsymbol{Z}}^{\alpha}_{n+1})$ and using Eq.(3.29), we can write the elastic strains at t_{n+1} given by Eq.(3.28) as

$$\boldsymbol{\epsilon}^{e}_{n+1} = \underbrace{\hat{\boldsymbol{\epsilon}}^{e}_{n+1} + \Delta t \boldsymbol{d}_{n+1}}_{\boldsymbol{\epsilon}^{e\star}_{n+1}} - \Delta t \sum_{\alpha=1}^{N} \dot{\gamma}^{\alpha}_{n+1} \widetilde{\boldsymbol{P}}^{\alpha}_{n+1} \tag{3.31}$$

Here $\hat{\boldsymbol{\epsilon}}^{e}_{n+1} = \Delta\boldsymbol{R}^{e}\boldsymbol{\epsilon}^{e}_{n}\Delta\boldsymbol{R}^{eT}$ (rotated elastic strains at t_n) and $\boldsymbol{\epsilon}^{e\star}_{n+1}$ are the elastic predictor strains. From this equation, the deviatoric and isochoric parts of $\boldsymbol{\epsilon}^{e}_{n+1}$ can be expressed as

$$\mathrm{dev}\boldsymbol{\epsilon}^{e}_{n+1} = \mathrm{dev}\boldsymbol{\epsilon}^{e\star}_{n+1} - \Delta t \sum_{\alpha=1}^{N} \dot{\gamma}^{\alpha}_{n+1} \widetilde{\boldsymbol{P}}^{\alpha}_{n+1}, \qquad \epsilon^{e}_{kk,\,n+1} = \epsilon^{e\star}_{kk,\,n+1} \tag{3.32}$$

with

$$\mathrm{dev}\boldsymbol{\epsilon}^{e\star}_{n+1} = \Delta\boldsymbol{R}^{e}\mathrm{dev}\boldsymbol{\epsilon}^{e}_{n}\Delta\boldsymbol{R}^{eT} + \Delta t \mathrm{dev}\boldsymbol{d}_{n+1}, \qquad \epsilon^{e\star}_{kk,\,n+1} = \epsilon^{e}_{kk,\,n} + \Delta t\, d_{kk,\,n+1} \tag{3.33}$$

where $d_{kk,\,n+1} = \mathrm{tr}(\boldsymbol{d}_{n+1})$. Note here that while the deviatoric part of $\boldsymbol{\epsilon}^{e\star}_{n+1}$ depends on $\Delta\boldsymbol{R}^{e}$, a quantity determined during the constitutive iterations at each time step Δt, the corresponding volumetric component is readily computed and known at the beginning of the time increment since $\boldsymbol{d}_{n+1}$ is given. Equations (3.32)–(3.33) can be used in the elasticity relationships, Eqs.(3.9)–(3.10), written at t_{n+1} as

$$\widetilde{\mathbb{C}}^{e-1}_{d,\,n+1} : \mathrm{dev}\boldsymbol{\tau}_{n+1} = \mathrm{dev}\boldsymbol{\epsilon}^{e}_{n+1} + \widetilde{\mathbb{C}}^{e-1}_{d,\,n+1} : \widetilde{\boldsymbol{H}}^{e}_{n+1}\epsilon^{e}_{kk,\,n+1} \tag{3.34}$$

$$p_{\tau,\,n+1} = \widetilde{\boldsymbol{H}}^{eT}_{n+1} : \mathrm{dev}\boldsymbol{\epsilon}^{e}_{n+1} + \widetilde{M}^{e}_{n+1}\epsilon^{e}_{kk,\,n+1} \tag{3.35}$$

to obtain

$$\widetilde{\mathbb{C}}^{e-1}_{d,\,n+1} : \mathrm{dev}\boldsymbol{\tau}_{n+1} = \mathrm{dev}\boldsymbol{\epsilon}^{e\star}_{n+1} - \Delta t \sum_{\alpha=1}^{N} \dot{\gamma}^{\alpha}_{n+1} \widetilde{\boldsymbol{P}}^{\alpha}_{n+1} + \widetilde{\mathbb{C}}^{e-1}_{d,\,n+1} : \widetilde{\boldsymbol{H}}^{e}_{n+1}\epsilon^{e\star}_{kk,\,n+1} \tag{3.36}$$

$$p_{\tau,\,n+1} = \widetilde{\boldsymbol{H}}^{eT}_{n+1} : \mathrm{dev}\boldsymbol{\epsilon}^{e}_{n+1} + \widetilde{M}^{e}_{n+1}\epsilon^{e\star}_{kk,\,n+1} \tag{3.37}$$

On the other hand, the evolution equations for the rotation tensor $\boldsymbol{R}^{e}$, Eq.$(2.37)_2$, and the slip system hardness κ^{α}_{s}, Eq.$(2.37)_8$ (or better, Eq.(2.47)), are integrated using the exponential map [Simo & Hughes, 1998] and a backward Euler scheme, respectively,

$$\boldsymbol{R}^{e}_{n+1} = \exp\Big(\Delta t \widetilde{\boldsymbol{\Omega}}^{e}_{n+1}\Big)\boldsymbol{R}^{e}_{n}, \qquad \widetilde{\boldsymbol{\Omega}}^{e}_{n+1} = \boldsymbol{w}_{n+1} - \sum_{\alpha=1}^{N} \dot{\gamma}^{\alpha}_{n+1} \widetilde{\boldsymbol{Q}}^{\alpha}_{n+1} \tag{3.38}$$

$$\kappa^{\alpha}_{s,\,n+1} = \kappa^{\alpha}_{s,\,n} + \Delta t \hat{\Theta}_{\kappa}(\dot{\gamma}^{\alpha}_{n+1}, \kappa^{\alpha}_{s,\,n+1}) \tag{3.39}$$

where $\widetilde{\boldsymbol{Q}}_{n+1} = \mathrm{skew}(\widetilde{\boldsymbol{Z}}^{\alpha}_{n+1})$ and the term $\mathrm{skew}(\dot{\boldsymbol{\epsilon}}^{e}_{n+1}\boldsymbol{\epsilon}^{e}_{n+1})$ in Eq.(3.38) has been left out since it is typically small [Marin & Dawson, 1998].

Equations (3.36)–(3.39) represent a set of couple nonlinear algebraic equations for the unknowns ($\mathrm{dev}\boldsymbol{\tau}_{n+1}$, $p_{\tau,n+1}$, $\boldsymbol{R}^e_{n+1}$, κ^α_{n+1}), with Eq.(3.37) giving the volumetric response, while the other three equations representing the deviatoric behavior. Note that although both behaviors are coupled through the tensor $\widetilde{\boldsymbol{H}}^e_{n+1}$, the volumetric response could be determined once the deviatoric response is computed (the elastic strain $\epsilon^{e\star}_{kk,n+1}$ is known). Hence, we focus our attention on the procedure to solve Eqs.(3.36),(3.38)–(3.39). For this purpose, using these equations we can formally write the residuals

$$\mathcal{R}_1 = \widehat{\mathcal{R}}_1(\boldsymbol{\tau}_{n+1}, \boldsymbol{R}^e_{n+1}, \kappa^\alpha_{s,n+1}) = \widetilde{\mathbb{C}}^{e-1}_{d,n+1} : \mathrm{dev}\boldsymbol{\tau}_{n+1} - \mathrm{dev}\boldsymbol{\epsilon}^{e\star}_{n+1} + \Delta t \sum_{\alpha=1}^{N} \dot{\gamma}^\alpha_{n+1} \widetilde{\boldsymbol{P}}^\alpha_{n+1} - \widetilde{\mathbb{C}}^{e-1}_{d,n+1} : \widetilde{\boldsymbol{H}}^e_{n+1} \epsilon^{e\star}_{kk,n+1} = \boldsymbol{0} \tag{3.40}$$

$$\mathcal{R}_2 = \widehat{\mathcal{R}}_2(\boldsymbol{\tau}_{n+1}, \boldsymbol{R}^e_{n+1}, \kappa^\alpha_{s,n+1}) = \boldsymbol{R}^e_{n+1} - \exp\Big[\Big(\boldsymbol{w}_{n+1} - \sum_{\alpha=1}^{N} \dot{\gamma}^\alpha_{n+1} \widetilde{\boldsymbol{Q}}^\alpha_{n+1}\Big)\Delta t\Big] \boldsymbol{R}^e_n = \boldsymbol{0} \tag{3.41}$$

$$\mathcal{R}_3 = \widehat{\mathcal{R}}_3(\boldsymbol{\tau}_{n+1}, \boldsymbol{R}^e_{n+1}, \kappa^\alpha_{s,n+1}) = \kappa^\alpha_{s,n+1} - \kappa^\alpha_{s,n} - \hat{\Theta}_\kappa(\dot{\gamma}^\alpha_{n+1}, \kappa^\alpha_{s,n+1}) = 0 \tag{3.42}$$

A full Newton-Raphson (N–R) method would typically be used to solve Eqs.(3.40)-(3.42). However, in this work we use a two-level iterative scheme (staggering scheme), as presented by others [Kalidindi, *et al.*, 1992],[Marin & Dawson, 1998]. In the first level, the residual Eq.(3.40) is solved for $\mathrm{dev}\boldsymbol{\tau}_{n+1}$ using N–R method by keeping ($\boldsymbol{R}^e_{n+1}$, κ^α_{n+1}) at their best available estimate. The linearization of this residual with respect to $\mathrm{dev}\boldsymbol{\tau}$ leads to the following system of five equations to be solved iteratively at each time step for the components of $\Delta(\mathrm{dev}\boldsymbol{\tau}_{n+1})$

$$\Big(\widetilde{\mathbb{C}}^{e-1}_{d,n+1} + \Delta t \sum_{\alpha=1}^{N} \frac{\partial \dot{\gamma}^\alpha_{n+1}}{\partial \tau^\alpha_{n+1}} \widetilde{\boldsymbol{P}}^\alpha_{n+1} \otimes \widetilde{\boldsymbol{P}}^\alpha_{n+1}\Big) : \Delta(\mathrm{dev}\boldsymbol{\tau}_{n+1}) = -\mathrm{dev}\boldsymbol{\epsilon}^e_{n+1} + \mathrm{dev}\boldsymbol{\epsilon}^{e\star}_{n+1} - \Delta t \sum_{\alpha=1}^{N} \dot{\gamma}^\alpha_{n+1} \widetilde{\boldsymbol{P}}^\alpha_{n+1} \tag{3.43}$$

where we have used $\mathrm{dev}\boldsymbol{\epsilon}^e_{n+1} = \widetilde{\mathbb{C}}^{e-1}_{d,n+1} : (\mathrm{dev}\boldsymbol{\tau}_{n+1} - \widetilde{\boldsymbol{H}}^e_{n+1} \epsilon^{e\star}_{kk,n+1})$ obtained from Eqs.(3.34) and $(3.32)_2$. In matrix notation, Eq.(3.43) can be written as

$$\Big([\widetilde{\mathbb{C}}^{e-1}_d]_{n+1} + \Delta t \sum_{\alpha=1}^{N} \frac{\partial \dot{\gamma}^\alpha_{n+1}}{\partial \tau^\alpha_{n+1}} \{\widetilde{P}^\alpha\}_{n+1} \{\widetilde{P^\alpha}\}^T_{n+1}\Big) \{\Delta\tau'\} = -\{\epsilon^{e'}\}_{n+1} + \{\epsilon^{e\star'}\}_{n+1} - \Delta t \sum_{\alpha=1}^{N} \dot{\gamma}^\alpha_{n+1} \{\widetilde{P}^\alpha\}_{n+1} \tag{3.44}$$

with $\{\epsilon^{e'}\}_{n+1} = [\widetilde{\mathbb{C}}^{e-1}_d]_{n+1}(\{\tau'\}_{n+1} - \{\widetilde{H}^e\}_{n+1} \epsilon^{e\star}_{kk,n+1})$.

Once a N–R solution for the stresses $\mathrm{dev}\boldsymbol{\tau}_{n+1}$ has been obtained, the second level of the iterative procedure involves (i) a N–R solution for the hardness κ^α_{n+1} from Eq.(3.42)

keeping ($\text{dev}\boldsymbol{\tau}_{n+1}$, $\boldsymbol{R}^e_{n+1}$) fixed, and (ii) a simple update for the lattice rotation $\boldsymbol{R}^e_{n+1}$ using Eq.(3.41), or equivalently, Eq.(3.38). Details of this second-level iterative update can be found elsewhere [Marin & Dawson, 1998]. The initial guess for the iterative scheme is based on the viscoplastic solution ($\boldsymbol{\epsilon}^e = \mathbf{0}$) for $\text{dev}\boldsymbol{\tau}$, an explicit estimate (forward Euler scheme) for κ^α_s, and the exponential map scheme for $\boldsymbol{R}^e$ with $\widetilde{\boldsymbol{\Omega}}^e$ in Eq.(3.38) evaluated at t_n. The convergence criterion used for this two-level iterative scheme is based on the changes of the norm of $\text{dev}\boldsymbol{\tau}$ and κ^α_s. In the present calculations, iterations are carried out until changes in the norm of both $\text{dev}\boldsymbol{\tau}$ and κ^α_s are less than $10^{-4}\kappa_{s0}$, where κ_{s0} is the initial slip system hardness.

With the crystal variables ($\text{dev}\boldsymbol{\tau}_{n+1}$,$\boldsymbol{R}^e_{n+1}$,$\kappa^\alpha_{n+1}$) known, the pressure at t_{n+1} is obtained using Eq.(3.37), which in matrix notation is written as

$$p_{\tau,\,n+1} = \{\widetilde{H}^e\}^T_{n+1}\{\epsilon^{e\,\prime}\}_{n+1} + \widetilde{M}^e_{n+1}\epsilon^e_{kk,\,n+1} \tag{3.45}$$

Finally, the crystal Cauchy stress is computed as

$$\boldsymbol{\sigma}_{n+1} = \det(\mathbf{1} + \boldsymbol{\epsilon}^e_{n+1})\boldsymbol{\tau}_{n+1} \tag{3.46}$$

where

$$\boldsymbol{\tau}_{n+1} = \text{dev}\boldsymbol{\tau}_{n+1} + p_{\tau,\,n+1}\widetilde{\mathbf{1}}, \qquad \boldsymbol{\epsilon}^e_{n+1} = \text{dev}\boldsymbol{\epsilon}^e_{n+1} + \frac{1}{3}\epsilon^e_{kk,\,n+1}\widetilde{\mathbf{1}} \tag{3.47}$$

The summary of the integration scheme to update the stress and state variables is given in Box 1.

3.4 Consistent Elastoplastic Tangent Moduli.

The (material) tangent moduli plays an important role in implicit finite element procedures, where its use is essential to preserve the quadratic rate of convergence that characterizes Newton's method during the equilibrium iterations. In this section, we derive an approximate closed form solution of the tangent moduli by a *consistent* linearization of the integrated constitutive equations. The word "approximate" reflects the fact that the derivation will not consider the linearization of the rotation tensor $\boldsymbol{R}^e_{n+1}$, the elastic Jacobian $J^e_{n+1} = \det(\mathbf{1} + \boldsymbol{\epsilon}^e_{n+1})$, and the hardness $\kappa^\alpha_{s,\,n+1}$.

In this work, the tangent moduli can be defined as

$$\boldsymbol{c}^{ep}_{n+1} = \frac{1}{\Delta t}\frac{\mathrm{d}\boldsymbol{\sigma}_{n+1}}{\mathrm{d}\boldsymbol{d}_{n+1}} = \frac{1}{J^e_{n+1}\Delta t}\frac{\mathrm{d}\boldsymbol{\tau}_{n+1}}{\mathrm{d}\boldsymbol{d}_{n+1}} \qquad \longrightarrow \qquad \mathrm{d}\boldsymbol{\tau}_{n+1} = \underbrace{J^e_{n+1}\boldsymbol{c}^{ep}_{n+1}}_{\boldsymbol{c}^{ep}_{\tau,\,n+1}} : \mathrm{d}\boldsymbol{d}_{n+1}\Delta t \tag{3.48}$$

To derive the expression for $\boldsymbol{c}^{ep}_{\tau,n+1}$, we decompose the Kirchhoff stress at t_{n+1}, $\boldsymbol{\tau}_{n+1}$, into its deviatoric and isochoric components,

$$\boldsymbol{\tau}_{n+1} = \text{dev}\boldsymbol{\tau}_{n+1} + p_{\tau,\,n+1}\widetilde{\mathbf{1}} \tag{3.49}$$

where, from Eqs.(3.9)–(3.10) (or Eqs.(3.34)–(3.35)),

$$\mathrm{dev}\boldsymbol{\tau}_{n+1} = \widetilde{\mathbb{C}}^{e}_{d,n+1}:\mathrm{dev}\boldsymbol{\epsilon}^{e}_{n+1} + \widetilde{\boldsymbol{H}}^{e}_{n+1}\epsilon^{e}_{kk,n+1}, \quad p_{\tau,n+1} = \widetilde{\boldsymbol{H}}^{eT}_{n+1}:\mathrm{dev}\boldsymbol{\epsilon}^{e}_{n+1} + \widetilde{M}^{e}_{n+1}\epsilon^{e}_{kk,n+1} \tag{3.50}$$

with

$$\mathrm{dev}\boldsymbol{\epsilon}^{e}_{n+1} = \mathrm{dev}\hat{\boldsymbol{\epsilon}}^{e}_{n+1} + \Delta t\,\mathrm{dev}\boldsymbol{d}_{n+1} - \Delta t\sum_{\alpha=1}^{N}\dot{\gamma}^{\alpha}_{n+1}\widetilde{\boldsymbol{P}}^{\alpha}_{n+1}, \quad \epsilon^{e}_{kk,n+1} = \hat{\epsilon}^{e}_{kk,n+1} + \Delta t d_{kk,n+1} \tag{3.51}$$

where $\hat{\epsilon}^{e}_{kk,n+1} = \epsilon^{e}_{kk,n}$. The linearization of $\boldsymbol{\tau}_{n+1}$, Eq.(3.49), gives

$$\mathrm{d}\boldsymbol{\tau}_{n+1} = \mathrm{d}\,\mathrm{dev}\boldsymbol{\tau}_{n+1} + \mathrm{d}p_{\tau,n+1}\tilde{\mathbf{1}} \tag{3.52}$$

To linearize $\mathrm{dev}\boldsymbol{\tau}_{n+1}$ and $p_{\tau,n+1}$, Eqs.(3.50), we will held constant the quantities $\widetilde{\mathbb{C}}^{e}_{d,n+1}$, $\widetilde{\boldsymbol{H}}^{e}_{n+1}$, $\widetilde{M}^{e}_{n+1}$ and $\widetilde{\boldsymbol{P}}^{\alpha}_{n+1}$ since we are assuming a constant $\boldsymbol{R}^{e}_{n+1}$. Then, consider first the linearization of $\mathrm{dev}\boldsymbol{\tau}_{n+1}$, Eq.(3.50)$_1$. This linearized equation can be written as

$$\widetilde{\mathbb{C}}^{e-1}_{d,n+1}:\mathrm{d}\,\mathrm{dev}\boldsymbol{\tau}_{n+1} = \mathrm{d}\,\mathrm{dev}\boldsymbol{\epsilon}^{e}_{n+1} + \widetilde{\mathbb{C}}^{e-1}_{d,n+1}:\widetilde{\boldsymbol{H}}^{e}_{n+1}\mathrm{d}\epsilon^{e}_{kk,n+1} \tag{3.53}$$

where, from Eq.(3.51),

$$\mathrm{d}\,\mathrm{dev}\boldsymbol{\epsilon}^{e}_{n+1} = \Delta t\widetilde{\mathbb{P}}_{d}:\mathrm{d}\boldsymbol{d}_{n+1} - \underbrace{\sum_{\alpha=1}^{N}\Delta t\frac{\partial\dot{\gamma}^{\alpha}_{n+1}}{\partial\tau^{\alpha}_{n+1}}\left(\widetilde{\boldsymbol{P}}^{\alpha}_{n+1}\otimes\widetilde{\boldsymbol{P}}^{\alpha}_{n+1}\right)}_{\widetilde{\mathbb{S}}_{n+1}}:\mathrm{d}\,\mathrm{dev}\boldsymbol{\tau}_{n+1}, \tag{3.54}$$

$$\mathrm{d}\epsilon^{e}_{kk,\,n+1} = \Delta t\tilde{\mathbf{1}}:\mathrm{d}\boldsymbol{d}_{n+1} \tag{3.55}$$

Using these two last equations, Eq.(3.53) can be written as

$$\left(\widetilde{\mathbb{C}}^{e-1}_{d,n+1} + \widetilde{\mathbb{S}}_{n+1}\right):\mathrm{d}\,\mathrm{dev}\boldsymbol{\tau}_{n+1} = \left\{\widetilde{\mathbb{P}}_{d} + \left(\widetilde{\mathbb{C}}^{e-1}_{d,n+1}:\widetilde{\boldsymbol{H}}^{e}_{n+1}\right)\otimes\tilde{\mathbf{1}}\right\}:\mathrm{d}\boldsymbol{d}_{n+1}\Delta t \tag{3.56}$$

or

$$\mathrm{d}\,\mathrm{dev}\boldsymbol{\tau}_{n+1} = \underbrace{\left(\widetilde{\mathbb{C}}^{e-1}_{d,n+1} + \widetilde{\mathbb{S}}_{n+1}\right)^{-1}:\left\{\widetilde{\mathbb{P}}_{d} + \left(\widetilde{\mathbb{C}}^{e-1}_{d,n+1}:\widetilde{\boldsymbol{H}}^{e}_{n+1}\right)\otimes\tilde{\mathbf{1}}\right\}}_{\widetilde{\mathbb{C}}^{ep}_{d,n+1}}:\mathrm{d}\boldsymbol{d}_{n+1}\Delta t \tag{3.57}$$

where $\widetilde{\mathbb{C}}^{ep}_{d,n+1}$ is the approximate deviatoric algorithmic moduli. Consider next the linearization of the volumetric part of $\boldsymbol{\tau}_{n+1}$, Eq.(3.50)$_2$. We can write

$$\mathrm{d}p_{\tau,n+1} = \widetilde{\boldsymbol{H}}^{eT}_{n+1}:\mathrm{d}\,\mathrm{dev}\boldsymbol{\epsilon}^{e}_{n+1} + \widetilde{M}^{e}_{n+1}\mathrm{d}\epsilon^{e}_{kk,n+1} \tag{3.58}$$

Using the expressions for $\mathrm{d}\,\mathrm{dev}\boldsymbol{\epsilon}^{e}_{n+1}$ and $\mathrm{d}\epsilon^{e}_{kk,\,n+1}$, Eqs.(3.54)-(3.55), in Eq.(3.58) one obtains

$$\mathrm{d}p_{\tau,n+1} = \widetilde{\boldsymbol{H}}^{eT}_{n+1}:\left(\Delta t\widetilde{\mathbb{P}}_{d}:\mathrm{d}\boldsymbol{d}_{n+1} - \Delta t\widetilde{\mathbb{S}}_{n+1}:\mathrm{d}\,\mathrm{dev}\boldsymbol{\tau}_{n+1}\right) + \Delta t\widetilde{M}^{e}_{n+1}\tilde{\mathbf{1}}:\mathrm{d}\boldsymbol{d}_{n+1} \tag{3.59}$$

which, with the help of Eq.(3.57), can be simplified to

$$\mathrm{d}p_{\tau,\,n+1} = \underbrace{\left(\widetilde{\boldsymbol{H}}^{eT}_{n+1}{:}\widetilde{\mathbb{P}}_d + \widetilde{M}^{e}_{n+1}\tilde{\mathbf{1}} - \widetilde{\boldsymbol{H}}^{eT}_{n+1}{:}\widetilde{\mathbb{S}}_{n+1}{:}\widetilde{\mathbb{C}}^{ep}_{d,\,n+1}\right)}_{\widetilde{\boldsymbol{H}}^{ep}_{\mathrm{v},\,\mathrm{n+1}}}{:}\mathrm{d}\boldsymbol{d}_{n+1}\Delta t \tag{3.60}$$

where $\widetilde{\boldsymbol{H}}^{ep}_{\mathrm{v},\,\mathrm{n+1}}$ is the approximate volumetric algorithmic moduli. Substituting Eqs.(3.57) and (3.60) into Eq.(3.52), one obtains

$$d\boldsymbol{\tau}_{n+1} = \underbrace{\left(\widetilde{\mathbb{C}}^{ep}_{d,\,n+1} + \tilde{\mathbf{1}} \otimes \widetilde{\boldsymbol{H}}^{ep}_{\mathrm{v},\,n+1}\right)}_{\widetilde{\mathbb{C}}^{ep}_{\tau,\,n+1}} : d\boldsymbol{d}_{n+1}\Delta t \tag{3.61}$$

Therefore, the approximate material tangent moduli is given by

$$\widetilde{\mathbb{C}}^{ep}_{n+1} = J^{e-1}_{n+1}\widetilde{\mathbb{C}}^{ep}_{\tau,\,n+1} = J^{e-1}_{n+1}\left(\widetilde{\mathbb{C}}^{ep}_{d,\,n+1} + \tilde{\mathbf{1}} \otimes \widetilde{\boldsymbol{H}}^{ep}_{\mathrm{v},\,n+1}\right) \tag{3.62}$$

Note that when no coupling between the deviatoric and volumetric response exists, i.e., when $\widetilde{\boldsymbol{H}}^{e}_{n+1} = \mathbf{0}$ (cubic crystals), $\widetilde{\mathbb{C}}^{ep}_{n+1}$ reduces to

$$\widetilde{\mathbb{C}}^{ep}_{n+1} = J^{e-1}_{n+1}\left(\widetilde{\mathbb{C}}^{e-1}_{d,n+1} + \widetilde{\mathbb{S}}_{n+1}\right)^{-1} : \widetilde{\mathbb{P}}_d + J^{e-1}_{n+1}\widetilde{M}^{e}_{n+1}\tilde{\mathbf{1}} \otimes \tilde{\mathbf{1}} \tag{3.63}$$

Box 1. Integration Procedure for Crystal Plasticity Model

1. Given quantities:

$$\boldsymbol{d}_{n+1},\ \boldsymbol{w}_{n+1},\ (\mathrm{dev}\boldsymbol{\epsilon}^e_n, \epsilon^e_{kk,n}, \boldsymbol{R}^e_n, \kappa_{s,n}),\ (\mathbb{C}^e_{d0}, \boldsymbol{H}^e_0, M^e_0),\ \boldsymbol{C}_0,\ \boldsymbol{Z}^\alpha_0 = \boldsymbol{s}^\alpha_0 \otimes \boldsymbol{m}^\alpha_0$$

2. Initial estimate for $(\mathrm{dev}\boldsymbol{\tau}_{n+1}, \boldsymbol{R}^e_{n+1}, \kappa_{s,n+1})$:

   viscoplastic solution $\rightarrow$ $\mathrm{dev}\boldsymbol{\tau}_{n+1}$

   forward Euler approx. $\rightarrow$ $\kappa_{s,n+1}$

   exponential map with $\widetilde{\boldsymbol{\Omega}}^e_n$ $\rightarrow$ $\boldsymbol{R}^e_{n+1}$

3. Compute elastic volumetric strain $\epsilon^e_{kk,n+1}$:

$$\epsilon^e_{kk,n+1} = \epsilon^{e\star}_{kk,n+1} = \epsilon^e_{kk,n} + \Delta t\, \mathrm{tr}(\boldsymbol{d}_{n+1})$$

4. Start two-level iterative scheme to compute $(\mathrm{dev}\boldsymbol{\tau}_{n+1}, \boldsymbol{R}^e_{n+1}, \kappa_{s,n+1})$:

   (a) Compute $\boldsymbol{C}_{n+1}, \Delta\boldsymbol{R}^e_{n+1}$:

$$\boldsymbol{C}_{n+1} = \boldsymbol{R}^e_{n+1}\boldsymbol{C}_0, \quad \Delta\boldsymbol{R}^e_{n+1} = \boldsymbol{R}^e_{n+1}\boldsymbol{R}^e_n$$

   (b) Rotate $(\mathbb{C}^e_{d0}, \boldsymbol{H}^e_0, \boldsymbol{Z}^\alpha_0)$ to $(\widetilde{\mathbb{C}}^e_{d,n+1}, \widetilde{\boldsymbol{H}}^e_{n+1}, \widetilde{\boldsymbol{Z}}^\alpha_{n+1})$:

$$\widetilde{\mathbb{C}}^e_{d,n+1} = (\boldsymbol{C}_{n+1} \underline{\otimes} \boldsymbol{C}_{n+1}) : \mathbb{C}^e_{d0} : (\boldsymbol{C}_{n+1} \underline{\otimes} \boldsymbol{C}_{n+1})^T$$

$$\widetilde{\boldsymbol{H}}^e_{n+1} = \boldsymbol{C}_{n+1}\boldsymbol{H}^e_0\boldsymbol{C}^T_{n+1}, \quad \widetilde{\boldsymbol{Z}}^\alpha_{n+1} = \boldsymbol{C}_{n+1}\boldsymbol{Z}^\alpha_0\boldsymbol{C}^T_{n+1}$$

   (c) Compute deviatoric elastic strains $\mathrm{dev}\boldsymbol{\epsilon}^{e\star}_{n+1}, \mathrm{dev}\boldsymbol{\epsilon}^e_{n+1}$:

$$\mathrm{dev}\boldsymbol{\epsilon}^{e\star}_{n+1} = \Delta\boldsymbol{R}^e_{n+1}\mathrm{dev}\boldsymbol{\epsilon}^e_n\Delta\boldsymbol{R}^{eT}_{n+1} + \Delta t\, \mathrm{dev}\boldsymbol{d}_{n+1}$$

$$\mathrm{dev}\boldsymbol{\epsilon}^e_{n+1} = \widetilde{\mathbb{C}}^{e-1}_{d,n+1} : (\mathrm{dev}\boldsymbol{\tau}_{n+1} - \widetilde{\boldsymbol{H}}^e_{n+1}\epsilon^e_{kk,n+1})$$

   (d) 1st level – Compute new estimate for $\mathrm{dev}\boldsymbol{\tau}_{n+1}$:

   N-R method to solve Eq.(3.43) $\rightarrow$ $\mathrm{dev}\boldsymbol{\tau}_{n+1}$

   (e) 2nd level – Compute new estimates for $\kappa_{s,n+1}$ and $\boldsymbol{R}^e_{n+1}$:

   N-R method to solve Eq.(3.39) $\rightarrow$ $\kappa_{s,n+1}$

   exponential map, Eq.(3.38) $\rightarrow$ $\boldsymbol{R}^e_{n+1}$

   (f) Check convergence of two-level iterative scheme:

   Are the changes in $\mathrm{dev}\boldsymbol{\tau}_{n+1}$ and $\kappa^\alpha_{s,n+1}$ less than TOL?

   NO, return to step (a).

   YES, continue to step (5).

5. Update mean stress (pressure) $p_{\tau,n+1}$:

$$p_{\tau,n+1} = \widetilde{\boldsymbol{H}}^{eT}_{n+1} : \mathrm{dev}\boldsymbol{\epsilon}^e_{n+1} + \widetilde{M}^e_{n+1}\epsilon^e_{kk,n+1}, \quad \widetilde{M}^e_{n+1} = M^e_0$$

6. Update Cauchy stress $\boldsymbol{\sigma}_{n+1}$ using Eqs.(3.46)–(3.47).

   EXIT

4. Validation of the Numerical Implementation

The crystal constitutive equations, Eqs.(2.37), and the corresponding integration scheme, Box 1, have been implemented in both a material point simulator (*mps*) and a user material routine in the finite element code *Abaqus* [ABAQUS, 2004]. These two implementations are validated here by solving a number of problems involving (i) the response of an aggregate of crystals to different deformation histories (*mps*), (ii) the behavior of a single finite element under plane strain compression (*Abaqus*), and (iii) the deformation behavior of polycrystals and single crystals where each crystal is represented by one or more finite elements (*Abaqus*). Most of the examples are mainly focused on testing the performance of the model and its numerical implementation, with some remarks added regarding the behavior of polycyrstals. The last example (uniaxial compression of a single crystal) compares simulation results and experimental data.

4.1 Material Point Simulations.

The material point simulator evaluates the response of material points subjected to homogeneous deformation histories. Here, a material point is assumed to be comprised by a collection of crystals whose individual mechanical responses are linked to that of the material point using the extended Taylor hypothesis (see Remark 2). In this section, we validate the integration scheme and the corresponding computer code (*mps*) by calculating the response of the crystal aggregate to a number of loading histories, as prescribed by the nonzero components of the velocity gradient $\boldsymbol{l}$. Hence, the examples presented are deformation driven, with the prescribed deformation path being mainly deviatoric (no information about the volumetric response is obtained).

Specifically, we solve for the response of aggregates of face center cubic (FCC) and hexagonal closed packed (HCP) crystals under specified deformation paths. A particular aggregate consists of 256 initially randomly oriented crystals chosen from a uniform orientation distribution, Fig. 4.1. The crystals in the aggregate deform by crystallographic slip on well defined slip systems: for FCC crystals on the twelve $\{111\}\langle 111\rangle$ slip systems while for HCP crystals on the three $(0001)\langle 11\bar{2}0\rangle$ basal, three $\{10\bar{1}0\}\langle 11\bar{2}0\rangle$ prismatic and six $\{10\bar{1}1\}\langle 11\bar{2}3\rangle$ pyramidal slip systems. Because for HCP crystals, pyramidal slip typically exhibits higher

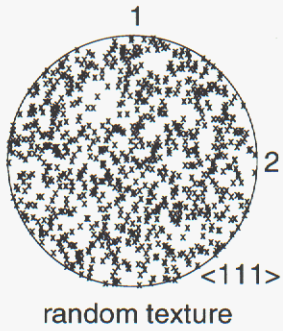

Figure 4.1: $\langle 111 \rangle$ pole figure for an initially random distribution of 256 crystal orientations.

Table 4.1: Material Parameters for Al7050

Elasticity Parameters

C_{11}	C_{12}	C_{44}
108.2 GPa	61.3 GPa	28.5 GPa

Viscoplasticity Parameters

m	$\dot{\gamma}_0$	h_0	$\kappa_{s,0}$	$\kappa_{s,S0}$	m'	$\dot{\gamma}_{S0}$
0.02	$1.0\,s^{-1}$	240.0 MPa	205.0 MPa	290.0 MPa	0.0	$5 \times 10^{10}\,s^{-1}$

Table 4.2: Material Parameters for Titanium

Elasticity Parameters

C_{11}	C_{12}	C_{33}	C_{44}	C_{13}
159.58 GPa	91.06 GPa	181.17 GPa	46.7 GPa	69.47 GPa

Viscoplasticity Parameters

m	$\dot{\gamma}_0$	h_0	$\kappa_{s,0}$	$\kappa_{s,S0}$	m'	$\dot{\gamma}_{S0}$
0.05	$1.0\,s^{-1}$	400.0 MPa	200.0 MPa	1000.0 MPa	0.005	$5 \times 10^{10}\,s^{-1}$

critical resolved shear stress than required for basal and prismatic slip, we assume that the strength of pyramidal slip is five times the strength of either basal or prismatic slip (both of which are taken to have equal strength). This relative strength ratio is maintained during deformation. Also, we specify an axial ratio $\frac{c}{a}$ of 1.63 (ideal value). Here, c and a are the lattice parameters of the HCP cell.

In the examples to be solved, we will track the stress response and / or texture evolution of the aggregate. Most of the stress-strain curves are presented in terms of macroscopic effective quantities $\sigma_e/\kappa_{s,0}$ and ε_e, where $\kappa_{s,0}$ is the initial slip system strength, and

$$\varepsilon_e = \int \sqrt{\frac{2}{3}} \parallel \mathrm{dev}\boldsymbol{D}_M \parallel dt, \qquad \sigma_e = \sqrt{\frac{3}{2}} \parallel \mathrm{dev}\boldsymbol{\Sigma}_M \parallel \tag{4.1}$$

with $\parallel (\bullet) \parallel = \sqrt{(\bullet):(\bullet)}$. Here, $\boldsymbol{D}_M$ and $\boldsymbol{\Sigma}_M$ are the macroscopic deformation rate and the macroscopic Cauchy stress, respectively. The deformation textures are shown in $\langle 111 \rangle$ pole figures for FCC and $\langle 0001 \rangle$ pole figures for HCP, with the global coordinate system indicated as $(1,2,3)$ or (x,y,z). The material constants used for anisotropic elasticity, Eqs.(3.7)–(3.8), the power–law kinetics, Eq.(2.42), and the hardening law, Eq.(2.47), correspond to those of polycrystal aluminum for FCC and polycyrystal titanium for HCP, and are presented in Tables 4.1 and 4.2, respectively.

The first two examples validate the integration scheme, Box 1, by comparing the stress response and texture predictions with those obtained from the viscoplastic version of the model [Mathur & Dawson, 1989]. In the first case, the aggregate of FCC crystals is deformed under plane strain compression ($l_{11} = -l_{33} = 1.0\,s^{-1}$; others $l_{ij} = 0$), while in the second case the same aggregate is subjected to simple shear loading ($l_{13} = 2.0\,s^{-1}$; others $l_{ij} = 0$). The computations are carried out using 150 increments with a constant time step of $\Delta t = 0.00866\,s$, to give a total effective strain of $\varepsilon_e = 1.5$ in plane strain compression and a total shear effective strain of $\gamma_e = 2.60$ ($\gamma_e = \sqrt{3}\varepsilon_e$) in simple shear. The computed stress response and texture evolution at three strain levels are presented in Fig. 4.2 for plane strain compression and Fig. 4.3 for simple shear. In general, the stress response shown in these figures differ little between the elasto-viscoplastic and viscoplastic computations. The effect of elasticity is most noticeable in the initial portions of the curves, where the crystal elasticity is predominant. However, at large strains, where all the crystals deform plastically, the stress level is mainly controlled by the strength or flow stress of the material, and hence the effect of elasticity is very small. Further, the textures predicted using both models are for all practical purposes the same. This means that elasticity has virtually no effect on texture evolution [Maniatty, *et al.*, 1992], [Marin & Dawson, 1996].

The effect of the time step on the accuracy of the predictions using the proposed numerical integration scheme is examined by computing the stress-strain response and texture development of the aggregate of HCP crystals when subjected to plane strain compression with $l_{11} = -l_{33} = 1.0\,s^{-1}$; others $l_{ij} = 0$. The aggregate response is obtained using effective strain increments of $\Delta\varepsilon_e = 0.1, 0.01, 0.001$ (time steps of $\Delta t = 0.086\,s, 0.0086\,s, 0.00086\,s$), to a total effective strain of $\varepsilon_e = 1.5$. The computed stress-strain response and the predicted textures at an effective strain of $\varepsilon_e = 1.5$ are given in Fig. 4.4. We observe that the stress

response converges to a unique curve as the time step is reduced. Also, the integration scheme is stable for the full range of time steps used, a behavior expected since he integration scheme is implicit, and hence the time step is limited by considerations of accuracy and convergence. On the other hand, the predicted texture is consistent with that expected for an HCP polycrystal undergoing plane strain compression [Cocks, *et al.*, 1998], and it is clear that the time step has little effect on the resulting texture.

As mentioned before, the proposed crystal plasticity model is a consistent extension of a rigid-viscoplastic model to include the effect of small elastic strains. Although the previous examples has validated the numerical implementation of the model, the influence of elasticity on the stress response was not pronounce because monotonic loading conditions were applied to the aggregate. In the next two examples, the aggregate of HCP crystals is deformed using deformation histories involving load path changes, and hence elastic effects will be more apparent. Specifically, a reverse loading test and a relaxation test are analyzed.

The reverse loading test is carried out by subjecting the aggregate to the uniaxial cyclic loading tension-compression-tension with a constant macroscopic strain rate of $\dot{\varepsilon}_e = 1.0\,s^{-1}$. The prescribed velocity gradients are $2l_{11} = 2l_{22} = -l_{33} = -1.0\,s^{-1}$, others $l_{ij} = 0$ for tension, and $2l_{11} = 2l_{22} = -l_{33} = 1.0\,s^{-1}$, others $l_{ij} = 0$ for compression. The direction of the load is reverse from tension to compression at a strain of $\varepsilon_{33} = 0.3$, and then from compression to tension at a strain of $\varepsilon_{33} = -0.1$. The response is determined using a constant time step of $\Delta t = 0.0086\,s$. The computed stress-strain curve for the 3–axis components is plotted in Fig. 4.5. One can clearly observe that, when the direction of loading is reversed, the material response is elastic until yielding occurs again on reloading. The increased hardening behavior observed after each reloading is due to the high rate of hardening of the material (see Fig. 4.5) as well as texture effects.

Finally, for the relaxation test, the aggregate is deformed under uniaxial compression with $2l_{11} = 2l_{22} = -l_{33} = 1.0\,s^{-1}$, others $l_{ij} = 0$, to an effective strain of $\varepsilon_e = 0.7$ (time $t = 0.7\,s$). At this point the applied load is reduced to zero ($l_{ij} = 0.0$) while keeping the effective strain at $\varepsilon_e = 0.7$. This case is analyzed with isotropic elasticity, using two different values of the elastic modulus: E and $5 \times E$, where $E = 9\mu_E K_E/(\mu_E + 3K_E)$ with μ_E and K_E being the effective shear and bulk moduli computed using Eq.(3.24) and the elastic material properties given in Table 4.2. The stress response during the loading and relaxation phases is computed with a constant time step of $\Delta t = 0.01\,s$ to a total time of $t = 1.5\,s$. The normalized effective stress versus time response is presented in Fig. 4.6.

Because of the viscous nature of the material model, the inelastic strains during relaxation increase with time at the expense of the reduction of the elastic strains. This is necessary to maintain the constant applied deformation. Hence, the stress level decays with time as the elastic strains relax, as shown in Fig. 4.6. This figure also shows that the magnitude of the elastic modulus affects the rate at which the stress reduces during relaxation. This is a direct consequence of the dependence of the relaxation time on ratio of the effective viscocity of the plastic behavior to the elastic modulus. Note that the magnitude of the elastic modulus also affects the initial portion of the stress response during the loading phase.

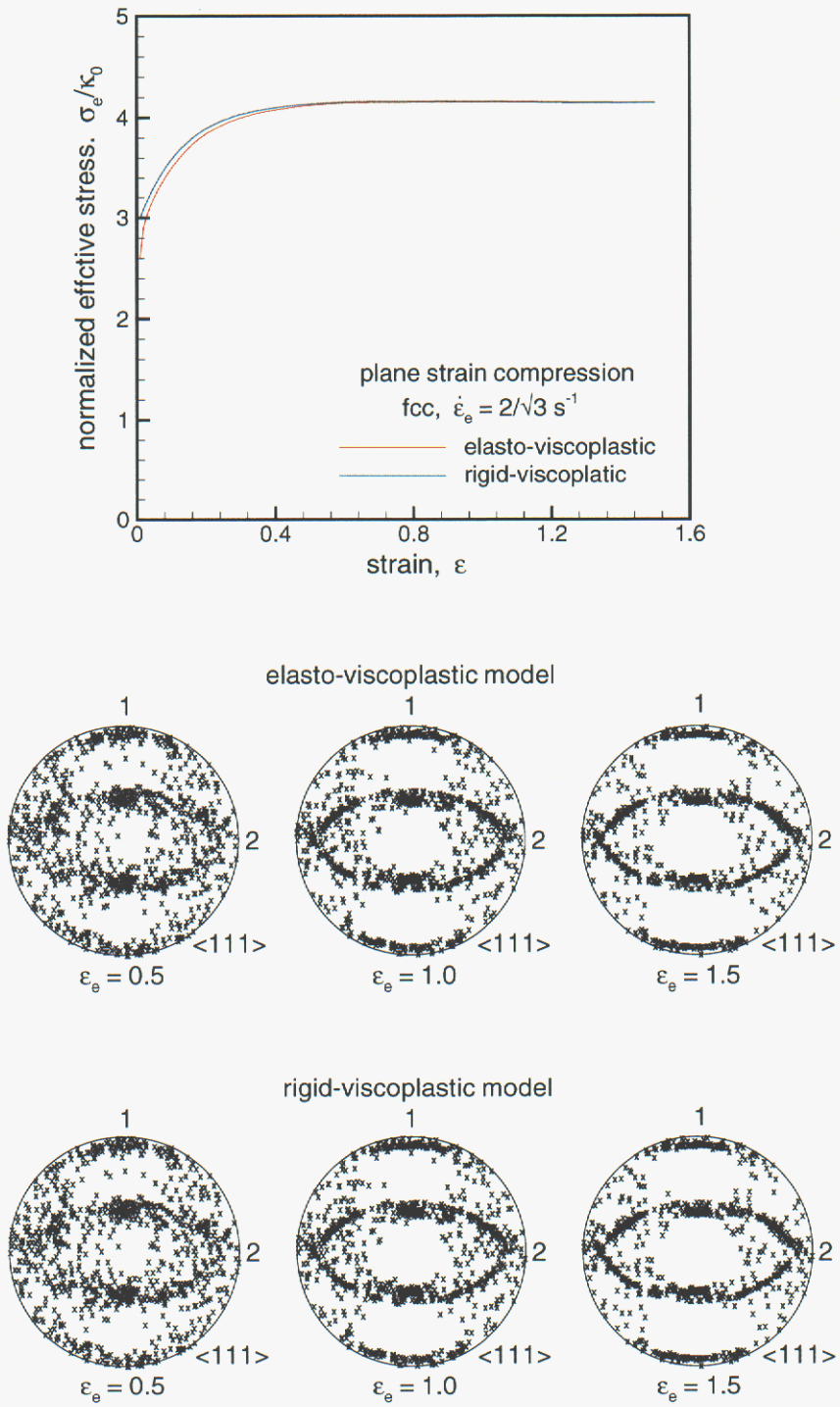

Figure 4.2: Macroscopic stress response and $\langle 111 \rangle$ pole figures at different strains for an aggregate of 256 FCC crystals subjected to plane strain compression computed using both the elasto-viscoplastic and rigid-viscoplastic models.

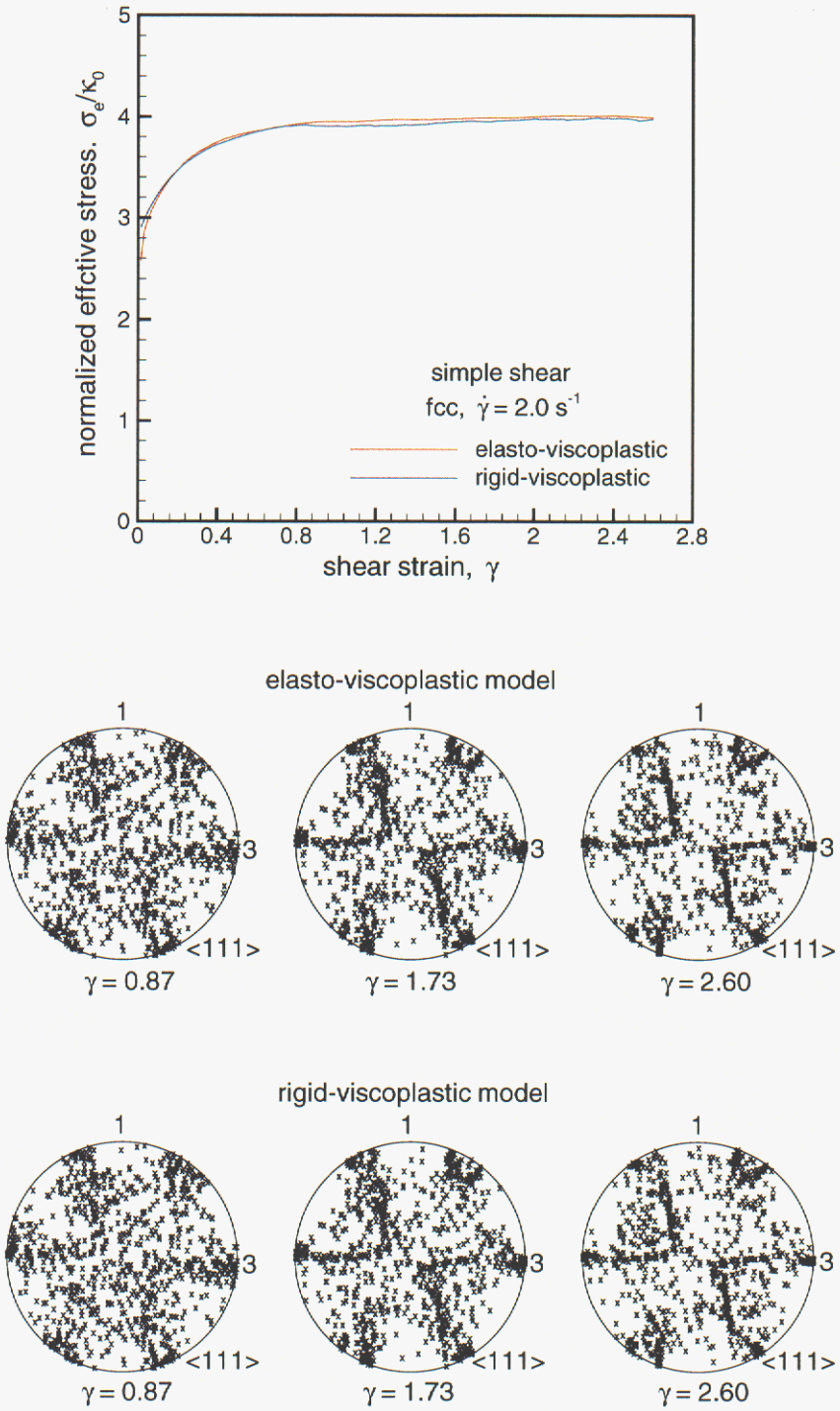

Figure 4.3: Macroscopic stress response and $\langle 111 \rangle$ pole figures at different strains for an aggregate of 256 FCC crystals subjected to simple shear computed using both the elasto-viscoplastic and rigid-viscoplastic models.

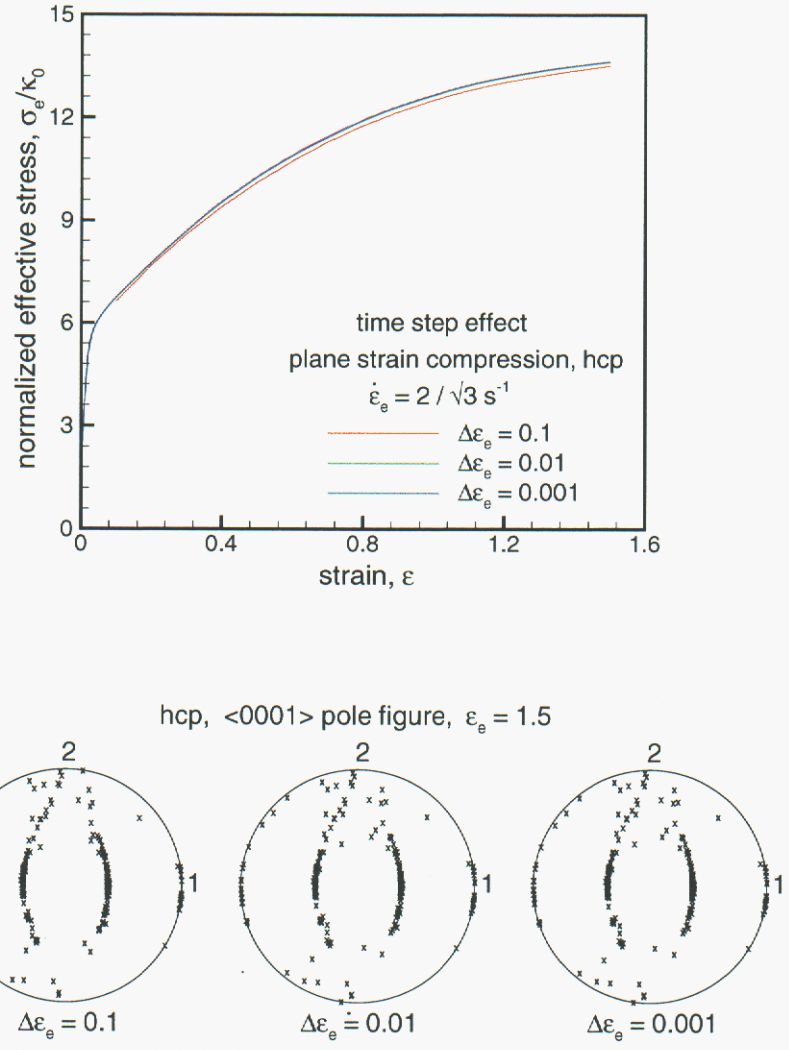

Figure 4.4: Macroscopic stress response and $\langle 0001 \rangle$ pole figure for plane strain compression of an aggregate of 256 HCP crystals computed using the elasto-viscoplastic model with constant time steps of $\Delta t = 0.086\ s, 0.0086\ s, 0.00086\ s$.

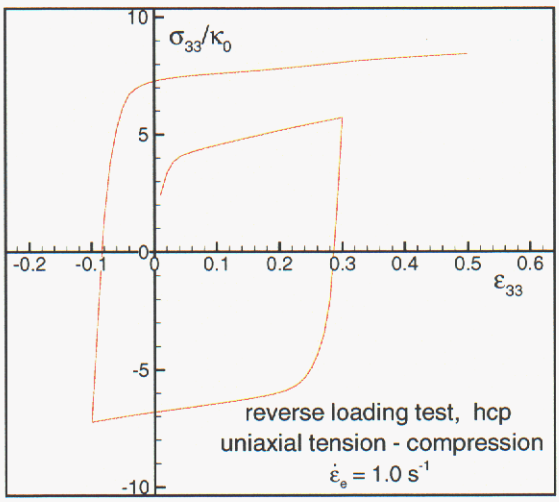

Figure 4.5: Macroscopic stress-strain response for a reverse (cyclic) loading test during uniaxial deformation of an aggregate of 256 HCP crystals. The load is reversed at $\varepsilon_{33} = 0.3$ (tension-compression) and $\varepsilon_{33} = -0.1$ (compression-tension).

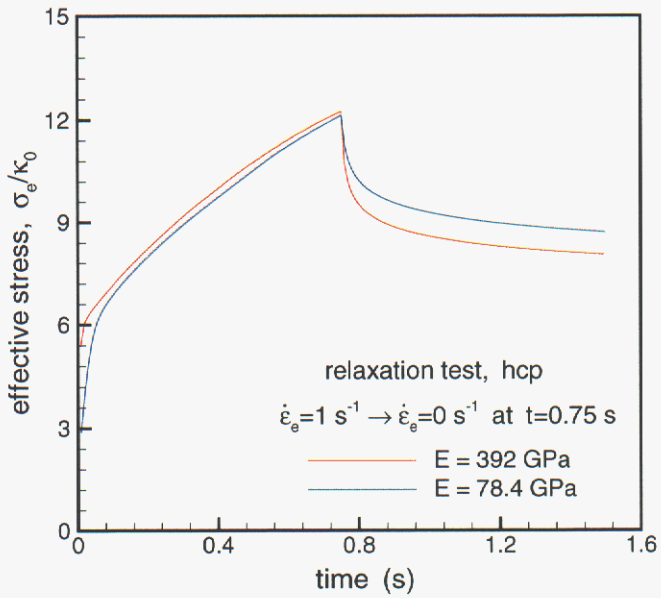

Figure 4.6: Macroscopic stress-strain response for a stress relaxation test during uniaxial compression of an aggregate of 256 HCP crystals. Two values of the elasticity modulus are used. The imposed macroscopic deformation is reduced to zero instantaneously.

4.2 ABAQUS Simulations.

The above computer program (*mps*) has been incorporated in the finite element code *Abaqus* as a material routine (*umat*) by creating the adequate interface to transform the vector representation of tensorial variables used in the *mps*, Eqs.(3.13)–(3.14), to the corresponding notation handled by *Abaqus*. This finite element implementation is being tested in this section by solving for the response of (*i*) a single element under plane strain compression where each computational point is associated with an aggregate of crystals, (*ii*) a polycrystal finite element model* under different loading paths where each element represents an individual crystal, and (*iii*) a single crystal under uniaxial compression, with the crystal represented with thousands of elements. Although the implementation has been carried out in both the implicit and explicit versions of *Abaqus*, here we mainly test the integration scheme in an implicit environment where the derived algorithmic material moduli, Eq.(3.62), will play a role in the convergence of the equilibrium iterations. All problems are three-dimensional (3–D).

In the first two examples, we validate the *Abaqus* implementation by comparing the response of a single finite element under plane strain compression with the corresponding results from the material point simulator. The *mps* runs are taken here as reference to validate the finite element implementation. The comparison metrics are the stress–time curves and texture evolution. The element used is an 8-noded brick element with reduced integration (*Abaqus* element type C3D8R). The computational point is assumed to consist of an ensemble of 256 crystals type FCC for the first case and type HCP for the second case. The corresponding material properties for each type of crystal are given in Tables 4.1 and 4.2. The initial crystal orientations ($\varepsilon_e = 0$) in the aggregate are randomly distributed, and the aggregate response is computed using the extended Taylor hypothesis. For the *mps* runs, the aggregate is subjected to a velocity gradient with components $l_{11} = -l_{33} = 1.0\,s^{-1}$; others $l_{ij} = 0$ ($\dot{\varepsilon}_e = 2/\sqrt{3}\,s^{-1}$). For the *Abaqus* simulations, the cube faces –y, +y, –x and –z are constrained to move along their normal directions, while a displacement boundary condition is applied along the +z face such as to obtain a constant macroscopic z–deformation rate of $-1\,s^{-1}$ (this results in a deformation state with $\dot{\varepsilon}_e \approx 2/\sqrt{3}\,s^{-1}$). In both the *mps* and the *Abaqus* runs the applied load is imposed during a time interval of $1.5\,s$, and the solution is obtained in 150 increments ($\Delta t = 0.01\,s^{-1}$).

The computed results are displayed in Figs. 4.7 and 4.8 for both FCC and HCP crystal aggregates, respectively. One can observe that the stress response obtained from both *mps* and *Abaqus*, for each type of aggregate, is almost the same. Note that these curves show increasing small differences as the deformation progresses, in particular for the HCP aggregate which has a higher hardening rate and a more anisotropic behavior. These differences

*The use of this idealized polycrystal with "bricks" representing the grain shape (microstructure) is mainly intended here to test the performance of the *Abaqus* numerical implementation. However, more realistic numerical microstructures should be employed when using crystal plasticity theory as a mesoscale approach to investigate actual material behavior at the grain–scale. These microstructures can be constructed using either Voronoi tessellation procedures or digitizing real microstructures, and meshed using adequate mesh generation software.

could be due to the specific details of the imposed loading: the *mps* simulations are fully kinematically driven, while the *Abaqus* runs use mixed boundary conditions (the +x face of the cube is stress–free). On the other hand, the predicted texture shown in both figures for the *Abaqus* and the *mps* runs at a strain of $\varepsilon_e = 1.73$ are, for all practical concerns, the same.

In the following examples, we will use the direct numerical simulation to study the behavior of crystal aggregates and single crystals. As mentioned before, this approach does not need any mean field hypothesis to partition the applied macroscopic deformation among the crystals of the aggregate, as such partition happens naturally as part of the finite element solution of the field equations. This specific feature generally introduces non-uniform deformation modes across elements or crystals that reproduces more realistic behaviors of polycrystalline aggregates. Specifically, here we study the deformation behavior and texture development of a polycrystalline aggregate under different loading paths and the response of a single crystal to uniaxial compression.

The polycyrstal aggregate contains 343 single crystals arranged in a cube of side l_0 consisting of $7 \times 7 \times 7$ 8-noded brick finite elements, see Fig. 4.9. The element type is the fully-integrated *Abaqus*–C3D8H[†] (8 integration points) which uses a hybrid (displacement-pressure) formulation to properly account for the incompressibility constraint emanating from the volume-preserving nature of plastic flow. Here, each element represents a crystal whose orientation is obtained from a uniform orientation distribution, as shown in the poles figures depicted in Fig. 4.9. As before, we will solve this problem for both FCC and HCP crystals and for three deformation histories: plane strain compression, uniaxial compression and simple shear. The material properties used for the crystal constitutive equations are the same as those used in the previous examples (Tables 4.1 and 4.2).

In these simulations, the plane strain compression loading is induced by constraining the motion of the –y, +y and –z cube faces along their normal directions (one point at the –z face needs to be fully constrained to eliminate rigid body motion). In addition, a variable displacement boundary condition is enforced on the +z face to obtain a constant z–axis macroscopic strain rate of $1\,s^{-1}$. For the uniaxial compression test, the –x, –y and –z cube faces are constrained to move along their normal directions, and a variable displacement boundary condition is applied on the +z face to give also a constant strain rate of $-1\,s^{-1}$ along the z–axis. Both of these cases induce macroscopic equivalent strain rates $\dot{\varepsilon}_e$ of approximately $2/\sqrt{3}\,s^{-1}$ for plane strain compression and $1\,s^{-1}$ for uniaxial compression. The load duration for both cases is $t = 1.5\,s$. On the other hand, for the simple shear test, the –z face is fixed, and a total displacement of $\dot{\gamma}_e\,t\,l_0$ is applied on the +z face along the +x direction. Here $\dot{\gamma}_e = 2\,s^{-1}$ is the prescribed shearing rate and $t = \sqrt{3}/2\,s$ is the duration of the load. The initial time step prescribed for these three cases are $0.01\,s$, $0.01\,s$, and $3/\sqrt{2} \times 10^{-2}$, respectively. However, during the solution procedure, *Abaqus* adjusted this time step for most of the runs based on convergence considerations. The average number of iterations at any increment for all the runs was between 3 and 4, meaning that the "approximate" algorithmic

[†]Typically, the less–expensive reduced integration elements, such as *Abaqus*–C3D8R, are used for simulations of large 3–D problems. The use of the *Abaqus*–C3D8H element in this relatively small 3–D example is just to test this element performance for crystal plasticity simulations.

material moduli derived in this work performs well during the equilibrium iterations. We note here that, although all simulations run to completion, in most of the cases the finite element meshes were highly distorted past a certain amount of strain. Hence, simulation results are mainly presented at strain levels where they are considered to still be "valid".

The results from the polycrystal simulations are presented in Figs. 4.10–4.11 for the FCC and HCP crystal aggregates, respectively. Each figure shows the deformed mesh and the aggregate texture for plane strain compression at $\varepsilon_e = 1.2$, for uniaxial compression at $\varepsilon_e = 1.0$, and for simple shear at $\gamma_e = 1.73$. The severely distorted meshes displayed in these figures clearly show the inhomogeneous deformation field that existed over the polycrystal during defomation. Such inhomogeneity in straining from crystal to crystal is mainly due to (*i*) the crystal anisotropic properties (elastic and plastic) and (*ii*) the difference in crystal orientation between neighboring crystals or elements (misorientation field). These two aspects introduce sharp variations in the constitutive response across elements (crystal interactions) that are reflected in the mesh deformation patterns shown by the deformed polycrystal. On othe other hand, the developed textures for each type of aggregate are consistent with those expected for each loading path. We note here that, although not pursue in this example, a comparison with the textures predicted by the extended Taylor model will show that the textures shown in Figs. 4.10–4.11 are typically more diffuse. This feature results from the heterogenous straining of the polycrystalline aggregate induced by the finite element discretization [Kocks, *et al.*, 1998].

As a last example, we predict the response of a single crystal under uniaxial compression. For this problem, we use part of the experimental data produced in a recent project [Hughes, *et al.*, 2000] to further validate both the numerical implementation and the crystal plasticity model. Specific metrics to use are the deformed shape of the sample, the stress-strain response, and the change in crystal orientation. In these experiments [Hughes, *et al.*, 2000], a cylindrical single crystal of 99.99% aluminum (FCC material) with dimensions $7.3\,mm \times 11.0\,mm$ (diameter and height) was compressed with the [421] crystal direction initially parallel to the compression axis, see Fig. 4.12. The test was conducted at room temperature, at a strain rate of $10^{-3}\,s^{-1}$ to a strain level of 0.6. The deformed shape of the crystal is also shown in Fig. 4.12, while the stress response and orientation changes plotted in an inverse pole figure are shown in Fig. 4.14, where the computed results described below are also given. As observed from the experimental results, the originally cylindrical single crystal ovalls during compression, a pattern consistent with single glide on average. This deformed shape reveals some degree of homogeneous deformation, and hence, the stress-strain curve is representative of the single crystal response and could be used to fit material parameters of the model (instead of the force-displacement curve). The inverse pole figure, on the other hand, depicts the breakup of the originally single crystal orientation. This breakup of the crystal into regions of different orientations reflects the formation of dislocation substructures (grain subdivision) [Hansen, *el al.*, 2001] and it is mainly driven by the deformation constraint imposed by the applied boundary conditions (compression platens).

The single crystal is modeled with 14976 brick finite elements, type *Abaqus*-C3D8R, see Fig. 4.13A. The sample reference frame, i.e., the axes 1–2–3 (or x–y–z), is oriented along

the crystal directions $[2\,1\,\overline{10}], [\overline{1}\,2\,0], [4\,2\,1]$, which gives the Euler angles of $\varphi_1 = 180^o, \phi = 77.4^o, \varphi_2 = 26.6^o$ (Kocks convention). Each finite element in the model is initialized with these Euler angles. The single crystal material properties used are given in Table 4.3. The plasticity parameters shown have been estimated from the experimental stress-strain curve using a coarse discretization of the crystal (48 elements). The computed results with the full finite element model should confirm this estimate. The quasi-static uniaxial compression loading is imposed by applying a variable negative displacement at the top of the cylinder along the z–axis ([421] crystal direction) to obtain a constant applied strain rate of $10^{-3}\,s^{-1}$. The bottom of the cylinder has a zero z–displacement, with two points on this surface completely fixed to avoid rigid body motions. The prescribed time interval and initial time step are $t = 600\,s$ and $\Delta t = 0.04\,s$, respectively. During the solution, *Abaqus* adjusted this time step in the range $\Delta t = 0.04\,s - 4.0\,s$. The solution was obtained in 294 increments, with an average number of equilibrium iterations per increment of 3.

Table 4.3: Material Parameters for Single Crystal Aluminum

Elasticity Parameters

C_{11}	C_{12}	C_{44}
108.2 GPa	61.3 GPa	28.5 GPa

Viscoplasticity Parameters

m	$\dot{\gamma}_0$	h_0	$\kappa_{s,0}$	$\kappa_{s,S0}$	m'	$\dot{\gamma}_{S0}$
0.01	$10^{-3}\,s^{-1}$	28.4 MPa	3.7 MPa	37.8 MPa	5.0×10^{-4}	$5 \times 10^{10}\,s^{-1}$

The numerical results are presented in Figs.(4.13)–(4.14). The deformed mesh, given in Fig 4.13B, clearly show that the crystal cross section ovals during deformation, as displayed by the experimental results. The long axis of this oval is parallel to the projection of the primary slip direction onto the compression plane. Also, the predicted stress-strain response presented in Fig. 4.14A agrees well with the experimentally determined curve. Here the stress has been computed as the volume average of the stresses in all the elements. As pointed out before, this prediction validates the estimated values of the plasticity material parameters given in Table 4.3 which were determined from a coarse mesh run. Note that the elastic portion of the curve is not well-captured, which may mean that the crystal elastic response determined from experiments is more compliant than the one predicted with the published values of the elastic parameters. Finally, from the inverse pole figure, one can see that the model predicts, as the experimental values show, the rotation direction of the compression axis towards the ideal stable orientation [011] [Courtney, 1990]. Although the relative spread (breakup) of these orientations is predicted qualitatively, the corresponding magnitude may not be yet compared quantitatively due to the small number of experimental points collected in the figure. Further studies are underway to complement the experimental data, and then, to assess "quantitatively" the predictive capability of the proposed crystal plasticity model. These studies include data generated from bicrystal samples as well [Hughes, *et al.*, 2000].

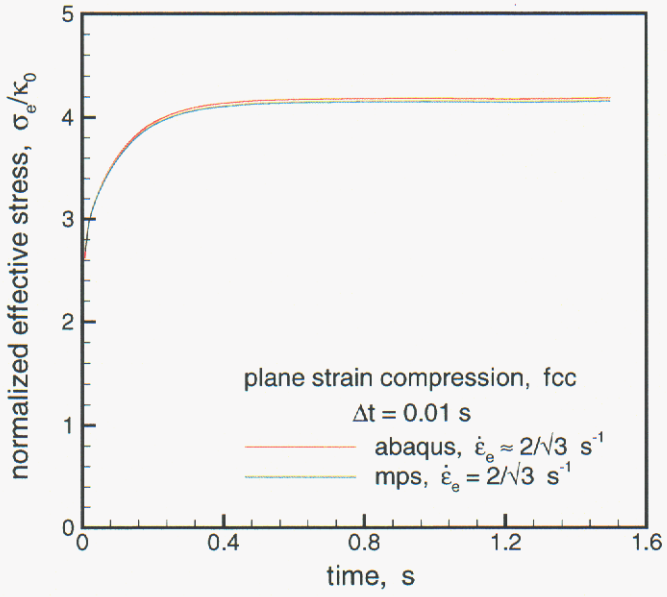

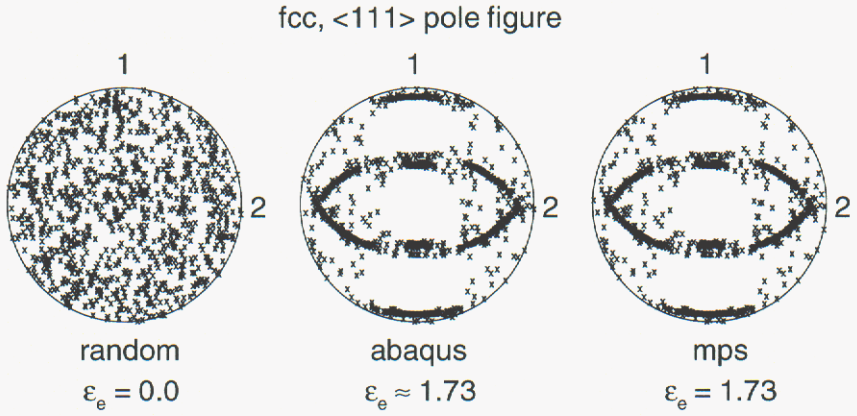

Figure 4.7: Macroscopic stress response and $\langle 111 \rangle$ pole figure for plane strain compression of an aggregate of 256 FCC crystals computed using the elasto-viscoplatic model with both *Abaqus* (one element) and *mps*.

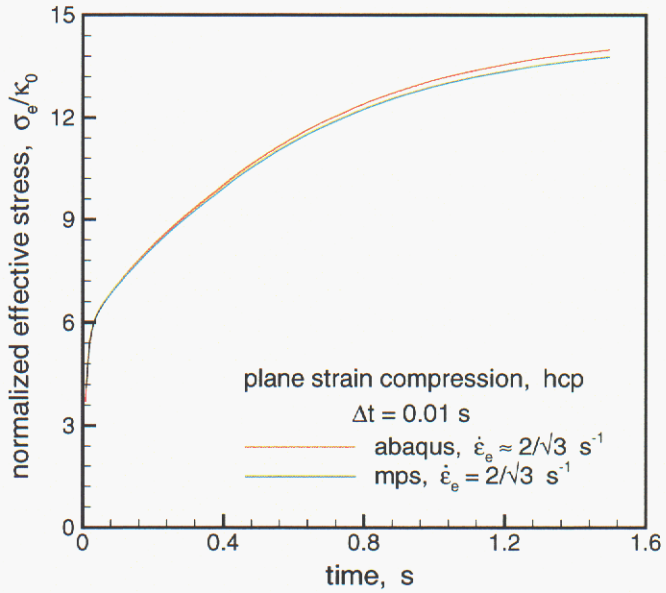

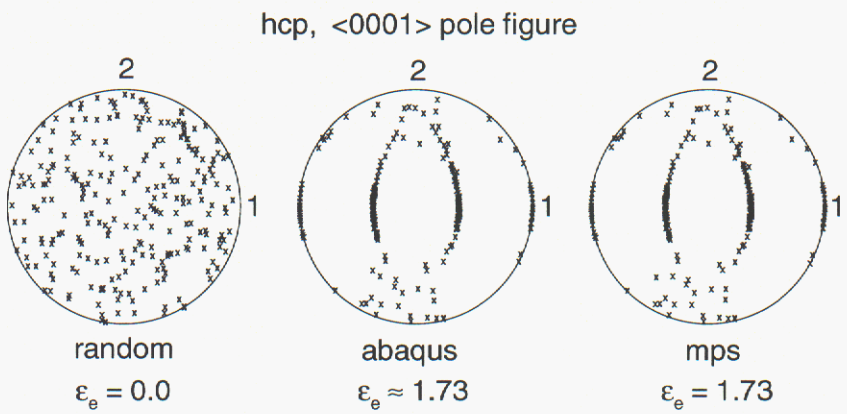

Figure 4.8: Macroscopic stress response and $\langle 111 \rangle$ pole figure for plane strain compression of an aggregate of 256 HCP crystals computed using the elasto-viscoplatic model with both *Abaqus* (one element) and *mps*.

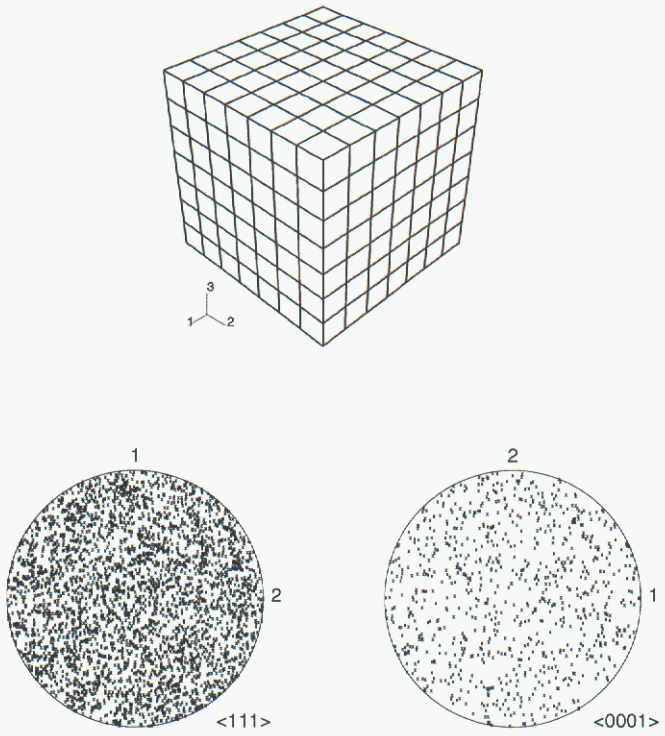

Figure 4.9: Finite element mesh of polycrystal model formed by $7 \times 7 \times 7$ C3D8H finite elements. Each finite element is a crystal with an orientation assigned from a random disdtribution as shown by the $\langle 111 \rangle$ (FCC) and $\langle 0001 \rangle$ (HCP) pole figures.

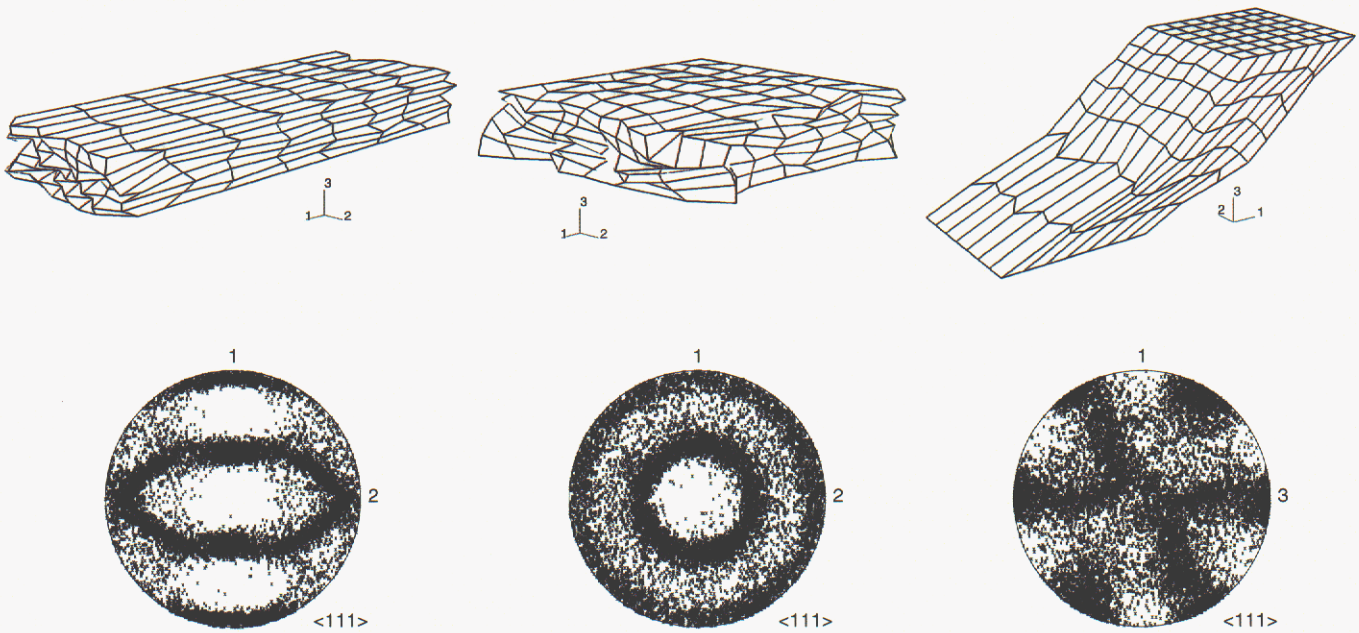

plane strain compression uniaxial compression simple shear

Figure 4.10: Deformed finite element meshes and $\langle 111 \rangle$ pole figures of FCC polycrystal deformed under plane strain compression ($\varepsilon = 1.2$), uniaxial compression ($\varepsilon = 1.0$) and simple shear ($\gamma_e = 1.73$).

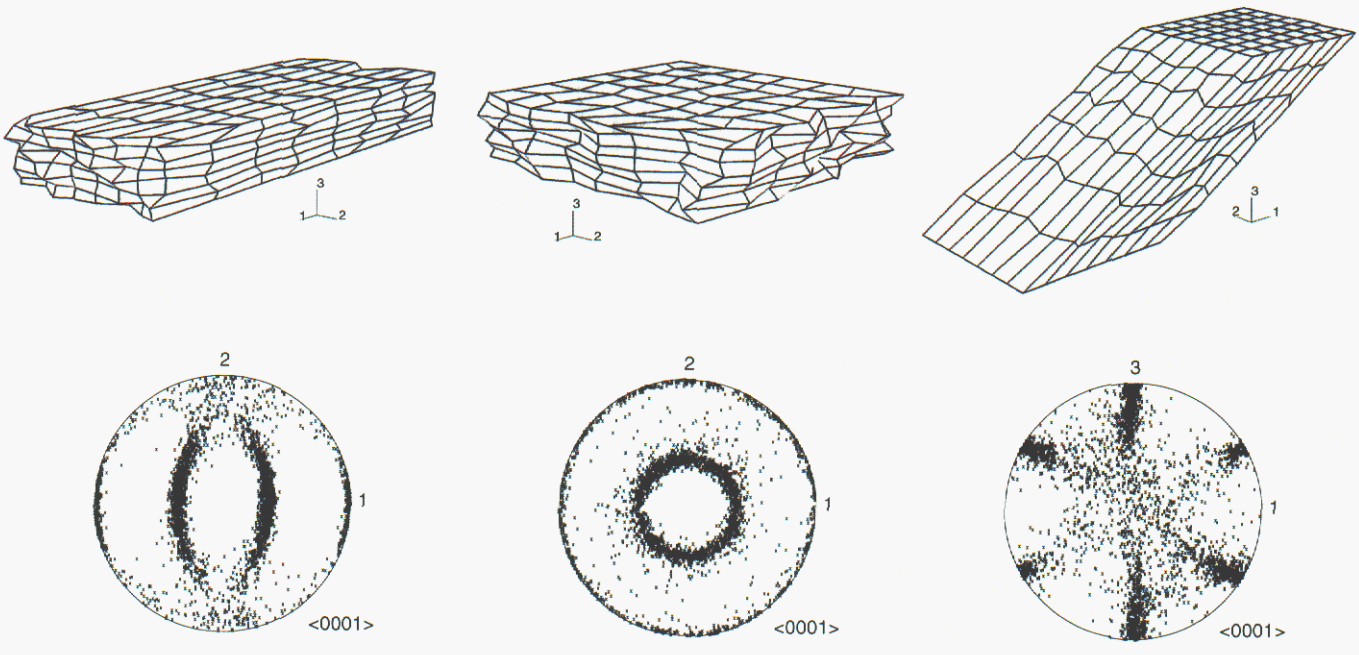

Figure 4.11: Deformed finite element meshes and $\langle 0001 \rangle$ pole figures of HCP polycrystal deformed under plane strain compression ($\varepsilon = 1.2$), uniaxial compression ($\varepsilon = 1.0$) and simple shear ($\gamma_e = 1.73$).

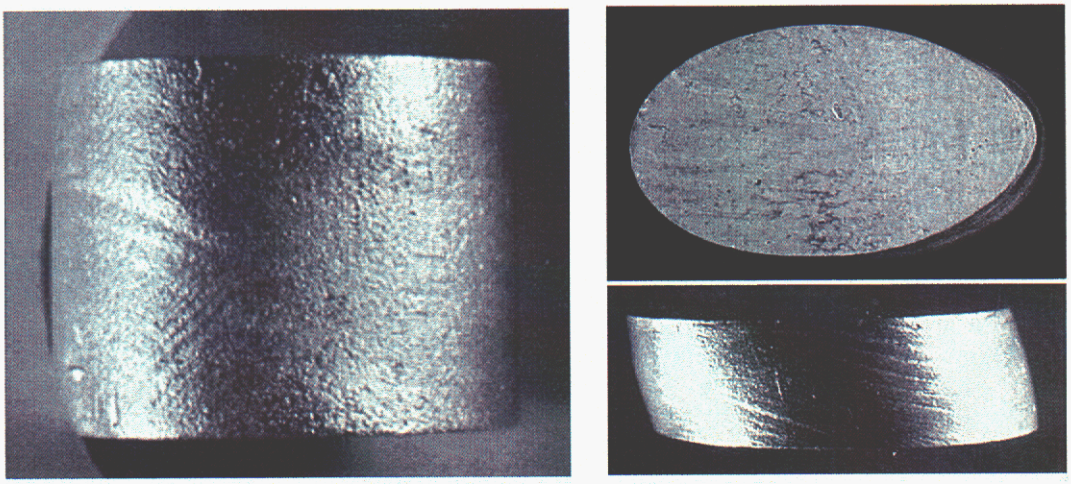

A *B*

Figure 4.12: (A) [421] single crystal used in the uniaxial compression experiments, and (B) compressed single crystal at a strain of 0.6 showing the ovaling of the cross section (after [Hughes, *el al.*, 2000]).

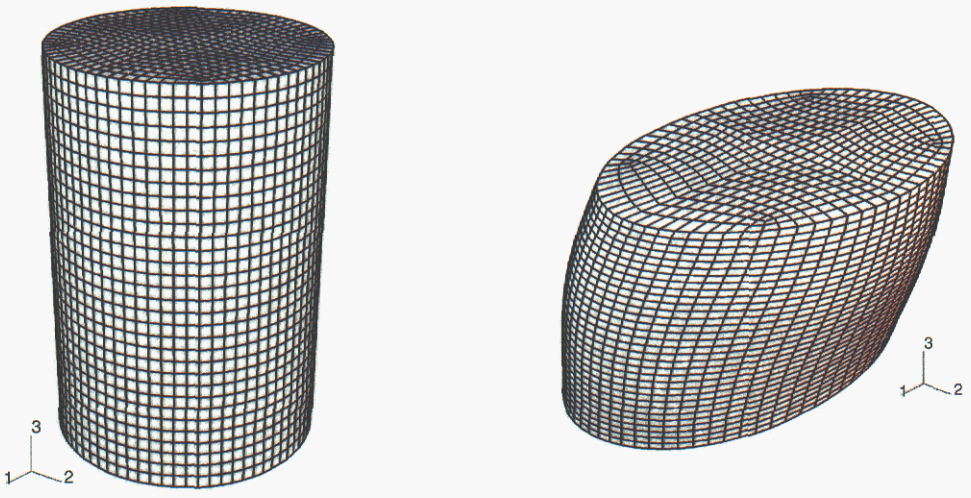

(A) (B)

Figure 4.13: (A) Undeformed finite element mesh for single crystal aluminum. The mesh consists of 14976 brick finite elements, type *Abaqus*–C3D8R. The initial Euler angles assigned to each element are $\varphi_1 = 180^o, \phi = 77.4^o, \varphi_2 = 26.6^o$ (Kocks convention). (B) Deformed crystal under uniaxial compression at $\varepsilon_z = 0.6$.

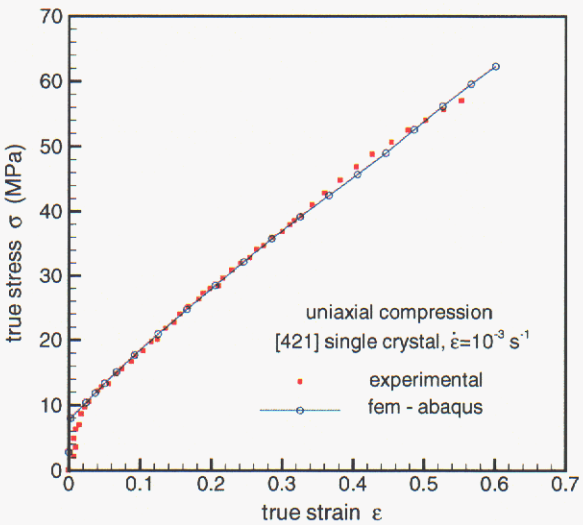

(A)

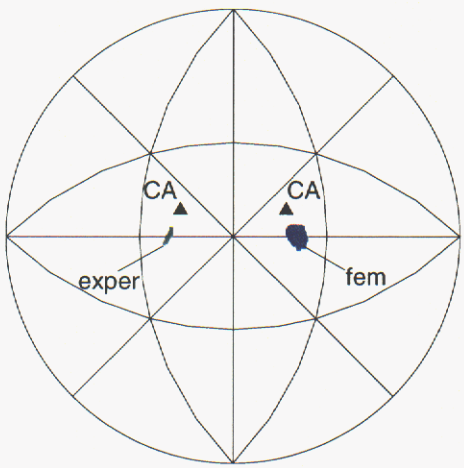

(B)

Figure 4.14: Comparison of experimental data and computed results: (A) Stress-strain response of single crystal under uniaxial compression, and (B) inverse pole figure plotted in a (001) stereographic projection, showing the crystal orientation of the compression axes (CA) at $\varepsilon_z = 0.6$ (note the breakup of the initial orientation indicated by the black triangle). For clarity purposes, the computed and experimental orientations have been plotted in equivalent stereographic triangles. In the standard triangle, the [421] CA tends to rotate, in an average, towards [110], an stable orientation with respect to the deformation.

5. SUMMARY

The formulation of a crystal plasticity model for small elastic strains and the corresponding integration procedure have been presented. As formulated, the model is suitable to represent the isothermal, anisotropic, and large deformation of polycrystalline aggregates (metals), and can be used as a mesoscale approach for grain–level materials modeling. A main feature of the formulation is that the crystal equations, which were developed in a thermodynamic framework, were written in the relaxed configuration $\widetilde{\mathcal{B}}$ defined by elastically unloading the deformed crystal without rotation from the current configuration to a stress–free state. The time integration scheme was implicit and used a staggered procedure to solve for the main variables of the model ($\mathrm{dev}\boldsymbol{\tau}$, p_τ, κ_s^α, $\boldsymbol{R}^e$). The numerical implementation in both a material point simulator and the finite element code *Abaqus* was validated by solving for the quasi-static deformation of FCC and HCP crystal aggregates under different isothermal loading conditions. The main metrics used for the validation of the model were crystal orientation evolution (texture), stress-strain response and deformed shape, although not all of them were used in each problem. The last example examined the predictive capability of the model by comparing computed results with experimental data from the uniaxial compression of a FCC single crystal.

As many other plasticity models presented in the literature [Peirce, *et el.*, 1983], [Kalidindi, *et al.*, 1992], [Cuitiño & Ortiz, 1992], [Steinmann & Stein, 1996], the proposed formulation used the multiplicative decomposition of the deformation gradient into elastic and plastic components. However, what distinguished the presented development from others is (*i*) the introduction of the polar decomposition of the elastic deformation gradient into the left stretch $\boldsymbol{V}^e$ and the rotation $\boldsymbol{R}^e$ tensors, and (*ii*) the use of the intermediate unloaded configuration defined by $\boldsymbol{V}^{e-1}$ to express the crystal constitutive equations. As mentioned before, this formulation followed the development presented by [Marin & Dawson, 1998] with a number of variations, in particular, modifications in the description of the crystal kinematics and changes in the numerical treatment of the resulting constitutive equations (time integration of the elastic strains).

Because the formulation is mainly intended for the direct numerical simulation of polycrystalline metals (small scale applications [Kocks, *et al.*, 1998]), not much emphasis was placed on describing mean field hypothesis or partitioning rules to relate the crystal–level response to the macroscopic behavior. Only the extended Taylor hypothesis was briefly mentioned since it was used to demonstrate the performance of the model and the integration procedure during the material point simulations. Also, as seen in the development,

the kinetics of plastic flow was described with the well–known power law function, and the evolution of the slip system strength was based on Voce's hardening rule. Current efforts are underway to improve such models to (i) explicitly account for thermally activated dislocation motion on slip kinetics and (ii) use better hardening rules with slip system interaction effects (latent hardening). Together with the inclusion of temperature effects, the improved model would allow us to capture rate– and temperature–dependent features of the deformation of polycrystalline aggregates.

One additional field of application of the proposed model is the prediction of the dynamic deformation of polycrystalline metals in the high-strain–rate and shock loading regime. This application requires the introduction of physics–based improvements of the model to capture two of the most relevant aspects of high–strain–rate induced deformation: pressure dependence of elastic–plastic deformation and phonon drag effects on slip kinetics. Such enhancements are currently being added to the model in the context of a new project [LDRD, 2006] aimed at using crystal plasticity as a grain–scale approach to capture the interplay between these high–strain–rate / shock wave phenomena and the heterogeneous microstructure of metals.

6. References

ABAQUS, Software Version 6.5 (2004), Hibbit, Karlsson, and Sorensen Inc.

Acharya, A., and Beaudoin, A.J., (2000), "Grain-Size Effect in Viscoplastic Polycrystals at Moderate Strains," *J. Mech. Phys. Solids*, 48:2213-2230.

Asaro, R.J., (1983), "Micromechanics of Crystals and Polycrystals," *Adv. Appl. Mech.*, 23:1–115.

Asaro, R.J., and Needleman, A., (1985), "Texture Development and Strain Hardening in Rate Dependent Polycrystals," *Acta Metall.*, 33:923-953.

Balasubramanian, S., and Anand, L., (2002), "Elasto-Viscoplastic Constitutive Equations for Polycrystalline FCC materials at Low Homologous Temperatures," *J. Mech. Phys. Solids*, 50:101-126.

Coleman, B., and Gurtin, M., (1967), "Thermodynamics with Internal State Variables," *J. Chem. Phys.*, 47:597-613.

Courtney, T.H., (1990), "Mechanical Behavior of Materials," McGraw Hill, Inc.

Cuitiño, A.M,, and Ortiz, M., (1992), "Computational Modeling of Single Crystals," *Modell. Simul. Mater. Sci. Engrg.*, 1:225-263.

Beaudoin, A.J., Dawson, P.R., Mathur, K.K., and Kocks, U.F., and Korzekwa, D.A., (1994), "Application of Polycrystalline Plasticity to Sheet Forming," *Comput. Methods Appl. Mech. Engrg.,*, 117:49-70.

Follansbe, P.S., and Kocks, U.F., (1988), "A Constitutive Description of the Deformation of Copper Based on the Use of the Mechanical Threshold Stress as an Internal State Variable," *Acta Metall.*, 36:81-93.

Frost, H., and Ashby, M., (1982), "Deformation Mechanism Maps," Pergamon Press.

Hansen, N., Huang, X., and Hughes, D.A., (2001), "Microstructural Evolution and Hardening Parameters," *Mat. Sci. Eng.*, A317:3-11.

Hughes, D.A., Bammann, D.J., Godfrey, A., Prantil, V.C., Holm, E.A., Miodownik, M.A., Chrzan, D.C., and Lusk, M.T., (2000), "Capturing Recrystallization of Metals with a Multi-Scale Materials Model," Sandia National Laboratories, CA, SAND2000-8232.

Kalidindi, S.R., Bronkhorst, C.A., and Anand, L., (1992), "Crystallographic Texture Evolu-

tion in Bulk Deformation Processing of FCC metals," *J. Mech. Phys. Solids*, 40:537-569.

Kocks, U.F., Argon, A.S., and Ashby, M.F., (1975) "Thermodynamics and Kinetics of Slip," *Prog. Mater. Sci.*, Pergamon Press.

Kocks, U.F., and Mecking, H., (1979) "A Mechanism for Static and Dynamic Recovery," *Strength of Metals and Alloys*, Haasen, P., Gerold, V., Kostorz, G., eds., Pergamon Press, 345-350.

Kocks, U.F., Tome, C.N., and Wenk. H.-R., (1998) "Texture and Anisotropy," *Cambridge University Press, first edition.*

Kok, S., Beaudoin, A.J., and Tortorelli, D.A., (2002), "A Polycrystal Plasticity Model Based on the Mechanical Treshold," *Int. J. Plast.*, 18:715-741.

Kothari, M., and Anand, L., (1998), "Elasto-Viscoplastic Constitutive Equations For Polycrystalline Metals: Application to Tantalum," *J. Mech. Phys. Solids* , 46:51-83.

LRDR Project, (2006), "Development of Simulation and Validation Techniques for the Dynamic Behavior of Metals at the Grain Scale," Tracy Vogler, PI.

Maniatty, A.M., Dawson, P.R., and Lee, Y.-S., (1992), "A Time Integration Algorithm for Elasto-Viscoplastic Cubic Crystals Applied to Modelling Polycrystalline Deformation," *Int. J. Numer. Methods Engrg.*, 35:1565-1588.

Marin, E.B., and Dawson, P.R., (1998), "On Modeling the Elasto-Viscoplastic Response of Metals using Polycrystal Plasticity," *Comput. Methods Appls. Mech. Engrg.,*, 165:1-21.

Mathur, K.K., and Dawson, P.R., (1989), "On Modeling the Development of Crystallographic Texture in Bulk Forming Processes," *Int. J. Plast.,*, 5:67-94.

Mecking, H., and Cocks, U.F., (1981) "Kinetics of Flow and Strain Hardening," *Acta Metall.*, 29:1865-1875.

Meyers, M.A., Vohringer, O., Kad, B.K., Xue, Q., Fu, H.-H., (2002), "Consitutive description of Dynamic Deformation: Physically-Based Mechanisms," *Material Science and Engineering,*, A322:194-216.

Peirce, D., Asaro, R.J., and Needleman, A., (1983), "Material Rate Sensitivity and Localized Deformation in Crystalline Solids," *Acta Metall.*, 31:1951-1976

Sarma, G.B., and Dawson, P.R., (1996), "Effects of Interactions Among Crystals on the Inhomogeneous Deformation of Polycrystals," *Act. Metall. Mater.,*, 5:1937-1953

Simo, J. C., and Hughes, T. J. R., (1998), "Computational Inelasticity," Springer.

Steinmann, P., and Stein, E., (1996), "On the Numerical Treatment and Analysis of Finite Deformation Ductile Single Crystal Plasticity," *Comput. Methods Appls. Mech. Engrg.,*, 129:325-354

DISTRIBUTION

External

1 Dr. N. Barton
Lawrence Livermore National Laboratory
P.O. Box 808, L-227
Livermore, CA 94551

3 Professor P.R. Dawson
Mechanical and Aerospace Engineering
196 Rhodes Hall
Cornell University
Ithaca, NY 14853

1 Dr. Youssef Hammi
Center for Advanced Vehicular Systems
Mississippi State University
Box 5405
Mississippi State, MS 39762

1 Professor M.F. Horstemeyer
Mechanical Engineering Department
Mail Stop 9552, 210 Carpenter Building
Mississippi State University
Mississippi State, MS 39762

1 Professor G.C. Johnson
Mechanical Engineering
6149 Etcheverry Hall
University of California
Berkeley, CA 94720-1740

1 Dr. P.J. Maudlin
Los Alamos National Laboratory
Group T{3, MS B216
P.O. Box 1663
Los Alamos, NM 87545

1 Professor M.P. Miller
Mechanical and Aerospace Engineering
194 Rhodes Hall
Cornell University
Ithaca, NY 14853

1 Mr. A. Oppedal
Center for Advanced Vehicular Systems
Mississippi State University
Box 5405
Mississippi State, MS 39762

1 Dr. G.P. Potirniche
Center for Advanced Vehicular Systems
Mississippi State University
Box 5405
Mississippi State, MS 39762

1 Professor R.A. Regueiro
Department of Civil, Environmental, and Architectural Engineering
University of Colorado at Boulder
Engineering Center ECOT 441, UCB 428
Boulder, CO 80309

1 Professor G.Z. Voyiadjis
Department of Civil and Environmental Engineering
Louisiana State University
Baton Rouge, LA 70803

Internal

1	MS 0372	J.T. Ostien, 1527
1	MS 0378	P.A. Taylor, 1435
1	MS 0384	H.S. Morgan, 9140
1	MS 0751	A.L. Fossum, 6117
1	MS 0751	R.M. Brannon, 6117

1	MS 0824	W.L. Hermina, 1510
1	MS 0889	S.V. Prasad, 1824
1	MS 0889	T.E. Buchheit, 1824
1	MS 1181	L.C. Chhabildas, 1647
1	MS 1181	T.J. Vogler, 1647
1	MS 1411	H.E. Fang, 1814
1	MS 1411	C.C. Battaile, 1814
1	MS 9042	D.M. Kwon, 8770
1	MS 9042	M.L. Chiesa, 8774
1	MS 9042	J.J. Dike, 8774
1	MS 9042	E.P. Chen, 8776
1	MS 9042	D.J. Bammann, 8776
1	MS 9042	A.A. Brown, 8776
1	MS 9042	J.W. Foulk III, 8776
1	MS 9042	J.A. Zimmerman, 8776
1	MS 9402	N.R. Moody, 8758
1	MS 9402	F.P. Doty, 8772
1	MS 9405	R.W. Carling, 8700
1	MS 9405	D.A. Hughes, 8776
5	MS 9405	E.B. Marin, 8776
1	MS 9405	T.D. Nguyen, 8776
1	MS 9409	R.E. Reese, 8776
2	MS 9018	Central Technical Files, 8944
1	MS 0899	Technical Library, 4536

This page intentionally left blank.